JGR Earth Surface

Key Points:
- We present an area-based framework to quantify river mobility across all river forms and processes
- We quantify the rates and scales of floodplain reworking and channel-thread reorganization for simulated and natural rivers
- The relative rates of channel thread reorganization and floodplain reworking vary systematically across river forms and processes

Author Contributions:
Conceptualization: Evan Greenberg, Vamsi Ganti
Data curation: Evan Greenberg, Austin J. Chadwick, Vamsi Ganti
Formal analysis: Evan Greenberg, Austin J. Chadwick
Funding acquisition: Vamsi Ganti
Investigation: Evan Greenberg, Austin J. Chadwick, Vamsi Ganti
Methodology: Evan Greenberg, Austin J. Chadwick, Vamsi Ganti
Project Administration: Vamsi Ganti
Software: Evan Greenberg
Supervision: Vamsi Ganti
Validation: Evan Greenberg, Austin J. Chadwick, Vamsi Ganti
Visualization: Evan Greenberg, Austin J. Chadwick, Vamsi Ganti
Writing – original draft: Evan Greenberg, Austin J. Chadwick, Vamsi Ganti

A Generalized Area-Based Framework to Quantify River Mobility From Remotely Sensed Imagery

Evan Greenberg[1] , **Austin J. Chadwick[1]** , and **Vamsi Ganti[1,2]**

[1]Department of Geography, University of California Santa Barbara, Santa Barbara, CA, USA, [2]Department of Earth Science, University of California Santa Barbara, Santa Barbara, CA, USA

Abstract Rivers are the primary conduits of water and sediment across Earth's surface. In recent decades, rivers have been increasingly impacted by climate change and human activities. The availability of global-coverage satellite imagery provides a powerful avenue to study river mobility and quantify the impacts of these perturbations on global river behavior. However, we lack remote sensing methods for quantifying river mobility that can be generally applied across the diversity of river planforms (e.g., meandering, braided) and fluvial processes (e.g., channel migration, avulsion). Here, we upscale area-based methods from laboratory flume experiments to build a generalized remote sensing framework for quantifying river mobility. The framework utilizes binary channel-mask time series to determine time- and area-integrated rates and scales of river floodplain reworking and channel-thread reorganization. We apply the framework to numerical models to demonstrate that these rates and scales are sensitive to specific river processes (channel migration, channel-bend cut-off, and avulsion). We then apply the framework to natural migrating and avulsing rivers with meandering and braided planforms. Results show that our area-based framework provides an objective and accurate means to quantify river mobility at reach- to floodplain-scales, which is largely insensitive to spatial and temporal biases that can arise in traditional mobility metrics. Our work provides a framework for investigating global controls on river mobility, testing hypotheses about river response to environmental gradients, and quantifying the timescales of terrestrial organic carbon cycling.

Plain Language Summary Rivers are the primary means by which water and sediment are delivered from the mountains to the ocean. Rivers are susceptible to climate change and human activities such as damming and deforestation. These ongoing and future impacts can influence how quickly rivers move across the floodplain, that is, river mobility. Because there are many kinds of rivers that move in a variety of ways, it is difficult to measure river mobility in a manner that is consistent for all rivers. This study overcomes this difficulty with a new method of analysis for satellite images, which builds upon recent advances in laboratory studies. We show that our measurements accurately capture how rivers move as they erode their banks, deposit sandbars, and periodically jump course. Our new methodology provides an opportunity to compare river mobility across the globe and identify regions where rivers are responding to climate change and human intervention.

1. Introduction

Alluvial rivers are dynamic and mobile landforms. From the timescale of a single flood to geologically paced environmental shifts, the positions, sizes, and shapes of alluvial rivers are in constant states of translation and deformation. These translations and deformations constitute the mobility of a river system. River mobility poses flood and erosion risks to more than 2.5 billion people living on large river floodplains (Best, 2019) and regulates the residence time of organic carbon in terrestrial environments (Repasch et al., 2021; Scheingross et al., 2021; Torres et al., 2017). Climate change and human modification are causing significant shifts in water and sediment fluxes at regional and global scales (Dethier et al., 2022; D. Li et al., 2021). However, the long-term impact of these changes on river mobility remains unconstrained.

River mobility encompasses morphodynamic processes active at spatial scales ranging from a single channel bank (bank-scale), multiple channel-bars (reach-scale), and ultimately across entire floodplains (floodplain-scale). The multi-scale nature of fluvial processes constitutes a hierarchy of landforms and active topography (e.g., Ganti et al., 2020). The process hierarchy can vary drastically across rivers. For example, meandering rivers feature bank-scale migration (Hickin & Nanson, 1984; Mason & Mohrig, 2019) and reach-scale channel-bend

Writing – review & editing: Evan Greenberg, Austin J. Chadwick, Vamsi Ganti

cutoff (Ashmore, 2013; Constantine & Dunne, 2008; Hooke, 2004), braided rivers evolve through bank-scale downstream bar accretion and reach-scale thread abandonment (Ashmore, 2013), and river delta channels periodically avulse at the floodplain-scale (Ashmore, 2013; Brooke et al., 2022; Ganti et al., 2014; Jerolmack & Swenson, 2007). Previous work has investigated mobility processes in different planform environments using numerical models (Chadwick et al., 2019, 2020; Ielpi et al., 2023; Jerolmack & Mohrig, 2007; H. K. Martin & Edmonds, 2022; Murray & Paola, 1997; Williams et al., 2016), physical experiments (Bryant et al., 1995; Chadwick et al., 2022; Ganti et al., 2016a, 2016b; Limaye, 2020; van de Lageweg et al., 2014), and detailed site-specific fieldwork (Dietrich & Smith, 1983; Micheli & Larsen, 2011).

The growing volume and availability of global-coverage multispectral remote imagery provides an unprecedented opportunity to study river behavior and test mechanistic insight gained from experiments and theory at global scales (Figure 1). This surge in data availability has motivated large-scale studies on river meandering (Ahmed et al., 2019; Constantine et al., 2014; Ielpi & Lapôtre, 2020) and river avulsion (Brooke et al., 2020, 2022; Valenza et al., 2020). However, most existing studies focus on a single mobility process (e.g., migration or avulsion) and are susceptible to timescale and spatial biases when comparing across varying measurement windows. Perhaps the most notable timescale bias is that shorter measurement windows result in systematically higher rates of river mobility (Donovan & Belmont, 2019), analogous to the Sadler effect documented in a variety of settings in geomorphology and sedimentology (Finnegan et al., 2014; Ganti et al., 2016b; Sadler, 1981; Sadler & Jerolmack, 2015). Spatial bias can also arise when mobility is measured over different length-scales because mobility can vary systematically along a given river reach (e.g., bend apices on a meandering river tend to migrate faster than straight sections) (Y. Li & Limaye, 2022).

Many of the existing methods to quantify river mobility from remote sensing are designed for single-thread meandering rivers and focus specifically on channel-bank migration (Donovan & Belmont, 2019; Donovan et al., 2021; Schwenk et al., 2017; Sylvester et al., 2019). Relatively few methods are designed for comparing river mobility across different river planforms, and generally limited to paired comparisons between two timesteps (Langhorst & Pavelsky, 2023; Nagel et al., 2022; Pekel et al., 2016; Rowland et al., 2016). This is problematic because multi-thread channels are pervasive worldwide and constitute some of the world's largest river systems (Galeazzi et al., 2021; Latrubesse, 2008). Existing morphology-independent methods are only designed to quantify bank-scale migration and ignore reach and floodplain scale processes like channel-bend cutoff and avulsion (e.g., Chadwick et al., 2023). There is a crucial need for planform-independent remote sensing methods that can integrate reach- and floodplain-scale river mobility, especially since these are the scales over which we expect natural environmental gradients and anthropogenic climate change to impact rivers.

Laboratory flume studies have developed methodologies for quantifying reach- and floodplain-scale river mobility (Bufe et al., 2019; Wickert et al., 2013). These methods are *area-based*, meaning that they quantify river mobility in terms of how the plan-view of channelized areas and unchannelized areas (i.e., floodplains) shift over time. Experimental area-based methods have been used to quantify the migration and avulsion of laboratory-scale (<1-m wide) braided rivers for hundreds of hours, allowing for the development of depositional landscapes (i.e., a simulated fluvial fan) and many cycles of fluvial-surface reworking (Hajek et al., 2014; Kim et al., 2006; J. Martin et al., 2009; Sheets et al., 2007; Tal & Paola, 2007). The analogous timescale for natural systems is on the order of hundreds to thousands of years (Ganti et al., 2020; Hajek & Straub, 2017)—timescales inaccessible by remote sensing. Furthermore, experimental area-based methods are designed in a dimensionless framework built with a knowledge of the true extent of the fluvial surface (i.e., the floodplain). In experimental settings, the fluvial surface generally grows to the size of the flume, but in natural rivers, this scale is difficult and sometimes impossible to constrain via remote sensing.

In this manuscript, we upscale area-based methodologies developed in experiments to the field-scale and present a generalized remote-sensing framework to quantify time- and area-integrated river mobility, which can be used to examine river behavior worldwide. Our proposed framework solves the single-process limitation of many other river mobility measurements by integrating across the morphodynamic hierarchy and simultaneously quantifies river mobility at the reach, and floodplain scales. Our framework characterizes the rates and areas over which (a) the floodplain is reworked and (b) the channel threads reorganize. We use numerical models of specific river processes to show that our metrics can accurately reproduce known rates of channel migration, channel-bend cutoff and avulsion. We then highlight example applications of our mobility framework to different river planforms (e.g., meandering and braided) and different river mobility processes (e.g., migration and
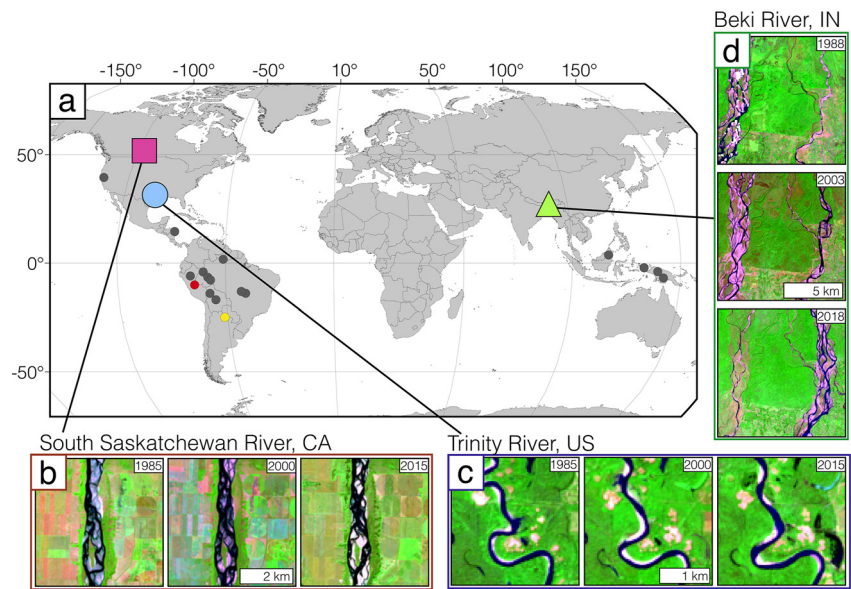
Figure 1. *Location map and example images of study reaches*. (a) World map with study reaches highlighted. Larger shapes are the rivers discussed in detail (Pink square—South Saskatchewan, Blue circle—Trinity, and Green triangle—Beki). Small gray circles are locations of meandering rivers highlighted in Section 3.2.3. Small red circle is the Ucayali River. Small yellow circle is the Rio Bermejo. Landsat images (SWIR, NIR, and Green RGB-composites) for the (b) South Saskatchewan River, (c) Trinity River, and the (d) Beki River avulsion.

avulsion). We conclude with an examination of the sensitivity and constraints of the framework with respect to its application to 37 years of Landsat data starting with Landsat 5. Together, area-based measurements that aggregate bank, bend, and avulsion scale processes can be leveraged to examine the sensitivity of river evolution in response to large-scale gradients in environmental signals and relate long-term river behavior to floodplain carbon storage.

2. Mobility Framework

Area-based mobility measurements were first developed in laboratory settings to evaluate the relative importance of water discharge, sediment flux, and basin subsidence in setting the pace of river mobility (Bufe et al., 2016, 2019; Cazanacli et al., 2002; Kim et al., 2010; Wickert et al., 2013). We upscale the area-based framework of Wickert et al. (2013) for remote sensing data, where river mobility is measured from time series of binary images representing the positions of the active river channel—called *channel masks*. We define two metrics: (a) *floodplain reworking*, which measures the cumulative reworking of the floodplain area and (b) *channel-overlap decay*, which measures channel reorganization in terms of the relative overlap of channelized areas between images. While the rates and areas obtained using our area-based metrics cannot be explicitly tied to specific river processes, they have the benefit of integrating across all reach- and bank-scale effects, providing a cumulative measurement of river mobility.

Our mobility measurements are made in a time-integrated framework from the series of channel masks. Consider a time series of n channel masks capturing the evolution of a river over some timeframe T. We use each of these channel masks as a baseline for comparison to subsequent images, whereby we consider river evolution from the baseline channel mask ($k \in [1, n-1]$) to the latest-available channel mask (i.e., nth image). For each baseline, we create image sets containing $i \in [0, n-k]$ images and $i = 0$ denotes the baseline channel mask. For each of these time series, we compare the baseline channel mask to every subsequent channel mask within the time series, which produces $\frac{n(n+1)}{2} - 1$ measurements for two mobility metrics. This approach is time-integrated because each of the n channel masks is used to compare with all channel masks that follow it, and mobility is quantified from the complete set of all combinations.
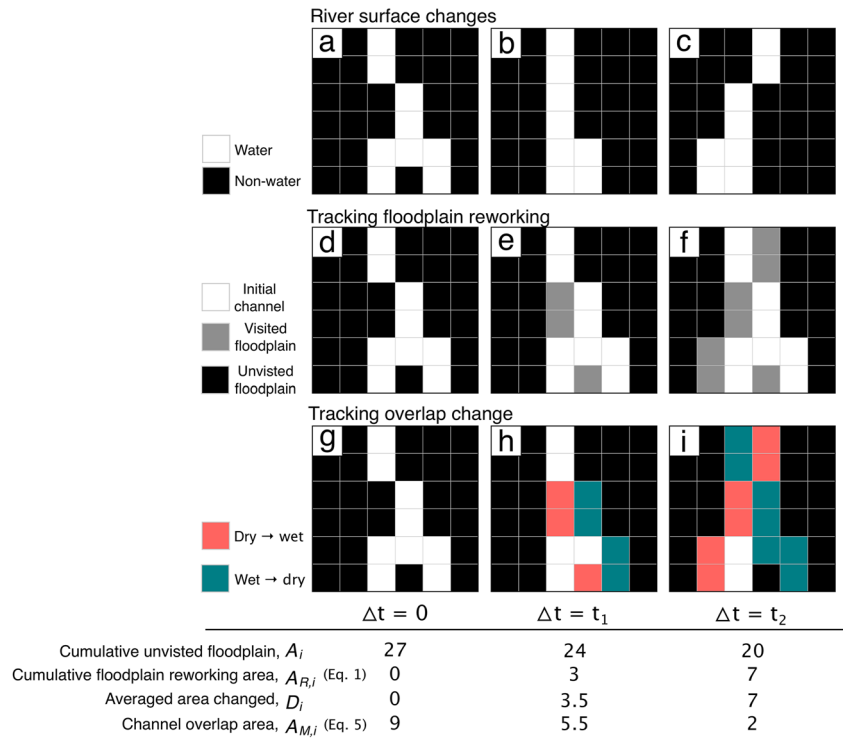
Figure 2. *Hypothetical application of the area-based mobility framework*. Changes are not meant to highlight any specific process. For the evolution of an arbitrary "river" from (a) $\Delta t = 0$, (b) t_1, and (c) t_2, we calculate the cumulative number of unvisited floodplain pixels, A_i, in panels (d–f) (black pixels). The cumulative reworking area, $A_{R,i}$ is calculated as the baseline floodplain area, A_d, here 27, subtracted by A_i. We also show the calculation of the average area changed, D_i in panels (g–i). The channel overlap area, $A_{M,i}$, is calculated as the baseline wetted area, A_w, here 9, subtracted by D_i.

2.1. Floodplain-Scale Mobility: Floodplain Reworking

Floodplain reworking captures the rates and scales at which the active channel accesses the floodplain. For a given baseline image k, we calculate the *cumulative reworked floodplain area* ($A_{R,i}$) in image i as follows:

$$A_{R,i} = A_d - A_i, \tag{1}$$

where A_d is the total area of dry pixels in the baseline channel mask and A_i is the dry-pixel area that has yet to be visited by the channel in the first i channel masks. The *cumulative reworked floodplain area*, $A_{R,i}$, is the dry-pixel area in the baseline channel mask that has been visited by channel water in Δt (Figure 2). The symbol Δt denotes the duration of river evolution captured by any arbitrary pair of images, and it varies from $\Delta t = 0$ (when a baseline image is compared to itself) to $\Delta t = T$ (when $k = 1$ is chosen as the baseline image and it is compared to the nth image). When a baseline image is compared to itself ($\Delta t = 0$) then none of the dry pixels have been visited, and so $A_d = A_i$ and $A_{R,i} = 0$. When the baseline image is compared to a later image with increasing Δt then more dry pixels will have been visited and so A_i will decrease compared to A_d ($A_d > A_i$) and $A_{R,i}$ will monotonically increase.

We repeat the computation in Equation 1 for different baseline images $k \in [1, n-1]$. We then take the ensemble average of $A_{R,i}$ across all k observations for every Δt to capture the characteristic growth in the cumulative floodplain reworking area over time. We describe the growth in floodplain reworking area using an exponential function:

$$\overline{A_{R,i}} = -P_R e^{-C_R \Delta t} + P_R, \tag{2}$$

where the overbar denotes the ensemble operator. Equation 2 has an *x*-intercept at 0 and grows at a rate, C_R [1/T], toward an asymptote P_R [L^2]. The growth constant C_R [1/T] represents the rate at which a river accesses the adjacent floodplain. In cases when the data are accurately modeled by Equation 2, the asymptote, P_R, provides a measure of the active floodplain area. Consequently, the 3-e-folding time of the growth constant, $\frac{3}{C_R}$, here called

the reworking timescale, T_R, represents the time necessary for the river to reach 95% of the estimated active floodplain size.

The estimated coefficients from Equation 2 describe the rate at which a river reworks previously non-water pixels (i.e., the floodplain) over time. However, it is not straightforward to directly compare these parameters across rivers. There is a scale-dependency in P_R where rivers with larger wetted areas have higher P_R values (Figure S1 in Supporting Information S1). Scale dependency is pervasive in river morphodynamic analysis and it is common practice to normalize parameters by a characteristic length scale, often the channel width (Hickin & Nanson, 1984). Laboratory applications of area-based mobility normalize measurements relative to the size of the experimental surface area (Bufe et al., 2019; Wickert et al., 2013), but we cannot apply the same normalization to natural rivers because the equivalent fluvial surface area is unknown. In our adaptation, P_R is an area (km^2) so we normalize by the median channel area $\overline{A_w}$. This provides an estimate of the active floodplain size in terms of the number of channel areas it contains, $\frac{P_R}{A_w}$ [–], here called the normalized active floodplain area, A_R^*. The parameter C_R and the corresponding reworking timescale are not scale dependent (Figure S1 in Supporting Information S1). A comparison between the reworking timescale and the normalized floodplain can help differentiate signals that arise from more extreme floodplain expansion or faster rates of reworking.

Traditional methods quantity bank migration using linear rates, which are either reported as the number of channel widths migrated per year or the time necessary to migrate one channel width (Constantine et al., 2014; Hickin & Nanson, 1984; Ielpi & Lapôtre, 2020). To compare our mobility rates with linear migration rates of rivers, we define a *linear floodplain reworking constant* [yr^{-1}] as follows:

$$R = C_R P_R / \overline{A_w}, \tag{3}$$

This constant is the absolute slope at the intercept of Equation 2 when normalized by $\overline{A_w}$.

2.2. Reach-Scale Mobility: Channel Overlap Decay

The channel overlap decay term describes the characteristic decay in the overlapping area of the river channel through time. We calculate the *channel overlap area* ($A_{M,i}$) for image $i \in [0, n-k]$ compared to baseline $k \in [1, n-1]$ following:

$$A_{M,i} = A_w - D_i, \tag{4}$$

where A_w is the wetted channel area in the baseline channel mask, and D_i is the area that has changed state when comparing the ith channel mask to the baseline channel mask ($D_i = [D_{i,\text{dry}-\text{wet}} + D_{i,\text{wet}-\text{dry}}]/2$ where the subscript denotes a change from dry to wet and vice versa). Unlike the unreworked area (A_i), the changed area (D_i) is not a cumulative measure but rather the area of the channel that is not overlapping between two images. The *channel overlap area*, $A_{M,i}$, is the channel area in the ith channel mask that did not change state when compared to the baseline channel mask (i.e., wet pixels remained wet; Figure 2). At $\Delta t = 0$ when $i = 0$, $D_i = 0$ and $A_{M,i} = A_w$. At $\Delta t > 0$ when $i > 0$, $D_i > 0$ and $A_{M,i}$ decreases with Δt. Like the calculations of $A_{R,i}$, we evaluate Equation 4 using $\frac{n(n+1)}{2} - 1$ pairs of channel masks by changing the baseline image.

We take an ensemble average of $A_{M,i}$ for every Δt and describe the decay using an exponential function:

$$\overline{A_{M,i}} = \left(\overline{A_w} - P_M\right)e^{-C_M \Delta t} + P_M \tag{5}$$

where C_M [1/T] is the decay rate and P_M [L^2] is the asymptote value. The asymptote, P_M, represents an estimated long-term memory of the channel area. In other words, P_M is the characteristic channel area that remains channel-area through time (i.e., a characteristic memory). This value should be low with significant channel-belt drift, and high when channel thread reorganization consistently returns the channel the previously visited locations. The 3-e-folding time of the decay constant, $3/C_M$, here called the overlap-decay timescale (T_M), represents the time necessary for the river network to lose 95% of its characteristic overlap. Together, P_M and C_M hold information about the area of planform consistency and the rate of channel thread re-organization.

We can use the estimated coefficients from Equation 5 to compare mobilities across rivers. To account for the scale dependence in P_M (Figure S1 in Supporting Information S1), we normalize P_M by the average channel area,

$\overline{A_w}$. We report $1 - \frac{P_M}{\overline{A_w}}$, called the normalized long-term decay area (A_M^*), to describe the normalized wetted channel area expected to change state. We can compare the overlap decay timescale and the normalized long-term decay area to describe the timescale of channel-thread overlap loss relative to the expected long-term shift in channel position. Finally, we also define a *linear channel-overlap-decay constant* as follows:

$$M = C_M \left(1 - P_M / \overline{A_w} \right) \tag{6}$$

which is the absolute slope at the intercept of Equation 5 when normalized by $\overline{A_w}$.

2.3. Challenges of River Scale and Stage in Reach-Scale Mobility Measurements

While our framework builds upon previous work (Bufe et al., 2019; Wickert et al., 2013), we had to make two important methodological considerations that enable general applicability to remotely sensed imagery. First, limited time sampling in remote sensing applications implies that the full extent of natural active fluvial surfaces (active floodplain) is often ambiguous. For example, only a fraction of the active floodplain area that may be worked by the river over centennial timescales may be captured over the maximum of 37 years starting with Landsat 5 data (Wulder et al., 2019). This is problematic because experimental metrics measure mobility relative to the normalized size of the experimental fluvial surface—a known and well-constrained quantity in laboratory applications, but an unknown in satellite observations. Here, we redefine the floodplain reworking and channel overlap decay terms such that they can be applied to natural rivers over remote sensing timescales without any a priori assumptions about the size of the fluvial surface area. In effect, scale is an open parameter within our analysis. We fit two scale terms, the estimated active floodplain area, P_R, and the long-term channel area memory, P_R, from the mobility measurements. Floodplain-scale processes can be directly compared to bank-scale processes using the area-normalized terms, R and M. We provide a more thorough examination of the scale in the sensitivity analyses (Sections 5.1 and 5.2).

The second primary consideration when upscaling the experimental framework to natural data is that channel masks for natural rivers will capture variations in river stage, while in the experimental applications, channel masks can be generated at consistent discharges. Mobility measurements taken from channel masks that capture variations in river stage may be misleading when variations in wetted channel area unrelated to mobility will be captured within the area-based metrics. Unfortunately, while there is no easy solution to this consideration, we suggest several techniques to minimize its effect. These include using median composites which average pixel surface reflectance values over multiple images, using data from similar periods of the hydrograph to capture consistent flood stages, or even omitting masks from the time series whose wetted areas significantly differ from the average. Additionally, long-term drift in wetted channel area could potentially bias mobility measurements. We use time-integrated baseline-comparisons to help mitigate against this potential source of bias. We provide an exploration into the susceptibility of the metrics to flood-stage variation in the sensitivity analyses (Section 5.3).

3. Materials and Methods

3.1. Application of the Framework to Numerical Models

Reduced complexity models of natural river processes have long provided insights into the controls on river mobility (Howard & Knutson, 1984; Liang et al., 2015; Murray & Paola, 1997; Sun et al., 1996). Here, we use numerical models to isolate and measure the relation between modeled rates of river mobility and the area-based mobility metrics presented in Section 2. Simulated binary raster data generated by numerical models are largely free of the natural variability that might confound applications to natural systems. We use the numerical models to validate the relation between "faster" and "slower" river mobility and our proposed floodplain reworking and overlap decay metrics.

3.1.1. Meandering River Model

We used a centerline evolution model to examine lateral migration and channel-bend cutoff in a simulated meandering river. For meandering rivers, where it is reasonable to assume that the evolution of the channel centerline reflects the coordinated trajectories of channel banks (Mason & Mohrig, 2019), centerline evolution models mimic the behavior of natural process. We used an implementation of a centerline evolution model (Howard &

Knutson, 1984) ported to Python (https://github.com/zsylvester/meanderpy) which accurately reflects natural observations that channel curvatures drive lateral migration rates (Sylvester et al., 2019). The model parameters allow us to explicitly set the lateral migration rates and the frequency of channel-bend cutoffs. Migration rates along the channel centerline are multiplied by a migration constant, kl, which sets the magnitude of lateral channel migration. Higher kl values correspond to higher migration rates for the same curvature. Thus, by varying kl, we set the river to migrate at different rates. Channel-bend cutoffs are included in the model as a threshold process whereby a channel bend will "cutoff" when the bend inlet and outlet portions of the centerline meet a predefined threshold proximity, cl.

We modeled the centerline evolution of a river with a constant width of 200 m and depth of 6 m over 40 bends. To examine different lateral migration rates, we ran the model with $kl \in [2, 4, 5, 10, 15, 20, 25]\ \left[\mathrm{m/yr}\right]$ and held $cl = 2$ (see Movie S1). To examine different cutoff thresholds, we ran the model with $cl \in [1, 2, 3, 4, 5, 6, 7, 8]$ with $kl = 25\ \mathrm{m/yr}$ (see Movie S2). For each run, we initialized the channel by running the model for 4,000 timesteps (timestep duration = 1/10th of a year) with $kl = 25$ and $cl = 2$ before running the model for an additional 4,000 timesteps with set values of kl and cl. We saved the x and y coordinates of the channel centerline every 10th iteration—corresponding to a yearly equivalent sampling—starting at the 700th timestep.

We made binary channel masks to measure the river mobility for each model run by projecting the centerline x and y coordinates onto a stationary 175 by 1,450 pixel grid with a top left corner at the model lifetime minimum x-coordinate and maximum y-coordinate and a bottom right corner at the model lifetime maximum x-coordinate and minimum y-coordinate. This produced 330 binary raster images with a resolution of roughly 31×31 m model equivalent. We then performed a 3-pass dilation of the binary centerline to produce a "river" of roughly 6-pixel width (186 m model equivalent). A channel-mask time series of 330 years is significantly longer than anything available for natural data. To make our model experiment comparable to natural data, we sampled 37-year blocks from the full set of channel masks to match the maximum length of the Landsat archive. For each 37-year block, we then measured the growth in $A_{R,i}$ and decay in $A_{M,i}$ and estimated the parameters P_R, C_R, P_M, and C_M. From these, we evaluate the functional dependence of T_R on A_R^* and T_M on A_M^* as well as the resulting R and M. We performed the 37-year sampling 20 times for each kl and cl value and report the median values in the resulting metrics.

3.1.2. Fan-Scale Avulsion Model

We used a cellular model of fan-scale river avulsion to examine the sensitivity of the mobility metrics to the occurrence and frequency of avulsions. Cellular avulsion models are driven by the super-elevation of channel-belts and topographic differences across the fan surface (Jerolmack & Mohrig, 2007). We used an implementation of a fan-scale avulsion model (H. K. Martin & Edmonds, 2022), which was designed to incorporate variable channel-belt reoccupation dynamics and variable avulsion trigger frequencies. We ran the model using different avulsion periods, $T_A \in [5, 10, 50, 100, 150, 200, 300, 500]$ yr, where higher T_A indicates less frequent frequencies (see Movie S3). Other model parameters were left constant (Table S1 in Supporting Information S1) to force the fan to evolve through compensational stacking (Straub et al., 2009)—new fan lobes preferentially build out in topographic lows—and eliminate the pre-dominance of channel reoccupation in guiding avulsion pathways. We ran the model for 100,000 years with a timestep of 10 years (10,000 iterations) and convert the model iterations into 1,000 binary raster images of channel-belt locations taken every 100 years. We subsample the 1,000 binary images into blocks of 40, which represent a model equivalent period of 4,000 years. This tends to capture sufficient avulsions for each avulsion trigger frequency such that representative mobility metrics can be calculated. For the blocks of 40 channel masks, we measured $A_{R,i}$ and $A_{M,i}$, estimated the parameters P_R, C_R, P_M, and C_M, and calculated the resulting R and M. We repeat the subsampling 20 times and report the median values of the resulting metrics.

There are two considerations in using this class of model to validate equivalent modern measurements. First, these models simulate channel-belts as a whole and do not resolve cross-sectional and channel bank-scale processes. Second, these models often simulate equivalent periods of time on the order of 10^5–10^6 years, which is not a naturally observable timeframe. Regardless, this class of fan-scale models are the only numerically efficient means to examine how variable avulsion frequencies alone correspond to our mobility metrics.

3.2. Application of the Framework to Remote Sensing Data

Our mobility framework can be applied to channel mask time series derived from multiple different sources (e.g., Landsat, Planet, Sentinel-2). Here, we utilized the Landsat archive, which has the longest freely available record

of multispectral surface reflectance and rich documentation of surface water analyses (e.g., Pekel et al., 2016). Landsat data also provide the best opportunity to quantify mobility across the globe at multi-decadal timescales. We focused on well-studied meandering and braided rivers, the Trinity and South Saskatchewan Rivers as well as a fan-scale avulsion from the Beki River, which provides a good counterpart to gradual migration processes. We describe below the methods used to generate input data sets of channel mask time series, how we define the area in which we evaluate the mobility, and how we specifically approached each example river process and type.

3.2.1. Generating Channel Mask Time Series From Landsat Data

We leveraged 37 years of multi-spectral atmospherically corrected surface reflectance data derived from the Landsat 5 and onwards to generate the time series of binary channel masks. There is a diversity of proven techniques to generate binary masks of surface water from remote imagery (Isikdogan et al., 2017, 2020; Jones, 2019; McFeeters, 1996; Pavelsky & Smith, 2008; Pekel et al., 2016; Rowland et al., 2016; Xu, 2006; K. Yang et al., 2014; X. Yang et al., 2019). While the specific method of generating input channel masks is not the focus of this study, the accuracy of correctly classified river water can impact river mobility measurements. Here, we followed the methodology used for USGS Dynamic Surface Water Extent (DSWE) products (Jones, 2019), which is an established technique to classify global surface water and is specifically designed for Landsat data. We generated channel masks using a two-step process that (a) generates a water mask indicating the presence or absence of surface water and (b) reduces the water mask to a channel mask that ideally only contains water associated with the active river system.

We used Landsat 5 TM, Landsat 7 ETM+ and Landsat 8 OLI/TIRS atmospheric corrected surface reflectance data sets available through Google Earth Engine (Gorelick et al., 2017) to generate water masks. Following Google Earth Engine's suggested strategy, we masked surface reflectance data for clouds and cloud shadows using the pixel quality assurance bands available in the Earth Engine-provided imagery ("Landsat Algorithms | Google Earth Engine, 2021"). From 1985 to 2021, we reduced the multiple images over a given area collected within each single year using a median aggregation. This provided annual median composite 7-band images across Blue to Shortwave-Infrared (SWIR) wavelengths (Figure 3a). We perform the median annual reduction on the assumption that if enough images are captured in a single year, the composite image minimizes intra-annual variability in river stage (Schwenk et al., 2017). With the annual composite images, we followed the methodology used for USGS DSWE products (Jones, 2019) as implemented in Python (X. Yang et al., 2019) to generate yearly composite products of surface water presence. The DSWE algorithm leverages a decision-tree structure between multiple spectral indices, and allows us to vary the threshold water level for each river and provides four different water classifications—high-confidence water, medium-confidence water, conservative partial surface water, and aggressive partial surface water (Figure 3b). We generated four channel masks corresponding to these four water classification thresholds and then manually selected the water classification confidence level that most accurately captured river surface water (Figure S2 in Supporting Information S1).

The DSWE algorithm provides products of classified surface water, which may include all types of inland waters. We reduced the surface water masks to channel masks following an established method (X. Yang et al., 2019), which geolocates the water mask raster product and collocates vector products of predicted channel location (Allen & Pavelsky, 2018; Yamazaki et al., 2019). We then defined a distance buffer (e.g., 1 km) between the predicted channel locations and the water mask and filter out any classified water that is not hydrologically connected to water adjacent to the predicted channel location. This procedure has been used with reliable success for global products of river properties (Langhorst & Pavelsky, 2023).

3.2.2. Quantifying Channel Overlap Decay and Floodplain Reworking Terms

We quantified the floodplain reworking and channel overlap from the channel masks derived from, at maximum, 37 years of Landsat data (e.g., 1985–2021). We defined an arbitrary study area for each study location that typically spans a cross-stream width larger than the apparent active channel-belt (or fluvial fan in the case of fans) and a downstream length of a characteristic reach-scale (at least three channel bends in a meandering river or 3 bar lengths in a braided river). The cross-stream length of the fluvial surface area does not have any effect on the mobility measurements (see Section 5.1). The downstream length of the fluvial area defines the length-scale over which river mobility is integrated. We first define the arbitrary fluvial surface area, then acquire yearly median composite images of the available Landsat data, and then generate channel masks through the methods outlined in Section 3.2.1.
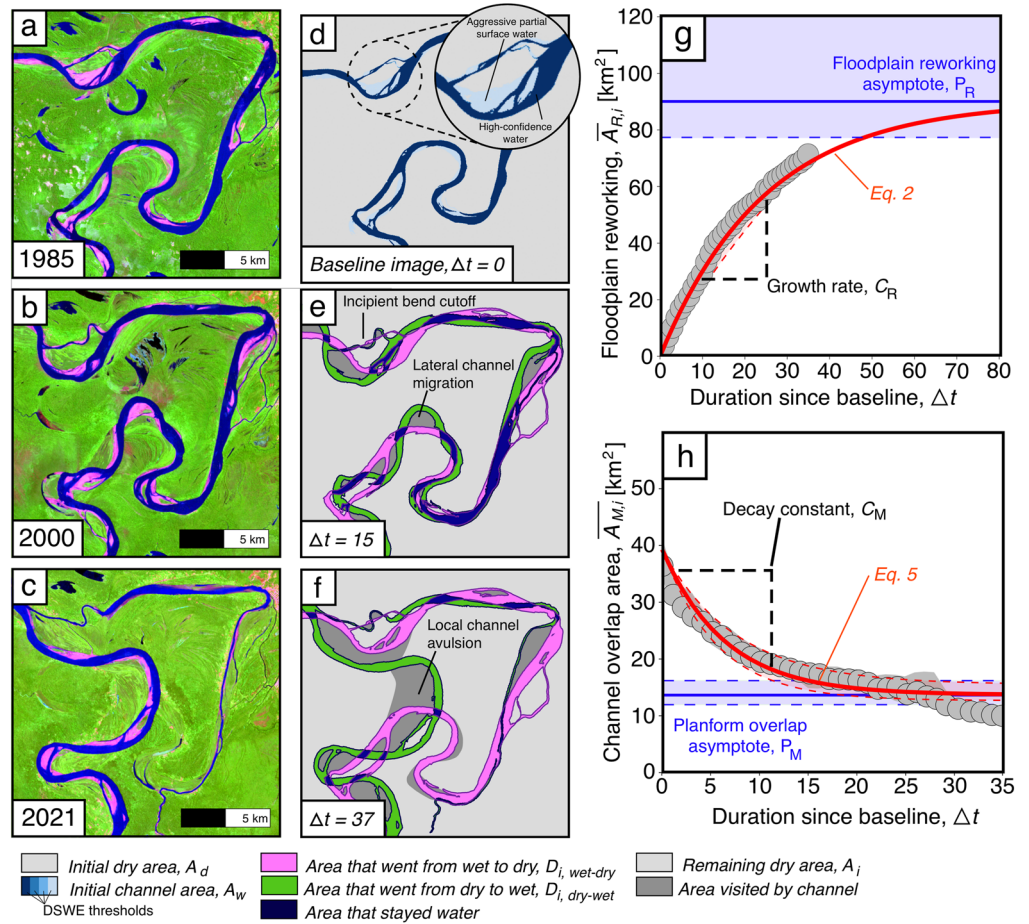
Figure 3. *Application of the mobility framework to natural data*. Landsat image (SWIR, NIR, Green) of the Ucayali River, Peru, in (a) 1985, (b) 2000, and (c) 2021. (d) Channel masks for varying Dynamic Surface Water Extent (DSWE) thresholds for the 1985 image, where the difference between the most and least conservative threshold is apparent. Pixel area changes between (e) 1985 and 2000, and (f) 1985 and 2021. We highlight specific river processes, which may be captured within the channel mask area. We used conservative partial surface water as the DSWE threshold for the representative channel mask for this reach. (g) Measured growth in $A_{R,i}$, where the gray circles are the median values ($\overline{A_{R,i}}$) and the gray area is the IQR with respect to Δt. The solid and dotted red lines are Equation 2 fits to $\overline{A_{R,i}}$, and 25th and 75th percentiles of $A_{R,i}$ with Δt, respectively. The projected floodplain reworking asymptote, P_R, and IQR are shown in blue. (h) Similar to (g) but showing the decay in $A_{M,i}$ with respect to Δt.

For each channel mask set, we measured $A_{R,i}$ (Equation 1) and $A_{M,i}$ (Equation 4) using the k baseline channel masks. We measured all values (A_w, A_d, A_i, D_i) in reference to the pre-defined fluvial surface. For example, A_w and A_d are the total baseline wetted area and baseline dry area within the defined fluvial surface, respectively. Similarly, A_i and D_i are the dry pixel area that hasn't been visited in first i channel masks, and the average area changed from water to dry or from dry to water, respectively (Figures 3a–3f). We then evaluated the 25th, 50th, and 75th percentiles of the reworked floodplain area, $A_{R,i}$, ($\overline{A_{R,i25th}}$; $\overline{A_{R,i50th}}$; $\overline{A_{R,i75th}}$) and channel overlap area, $A_{M,i}$, ($\overline{A_{M,i25th}}$; $\overline{A_{M,i50th}}$; $\overline{A_{i75th}}$) for a given Δt. We then fit Equations 2 and 5 using a least squares optimizer to the 25th, 50th, and 75th percentiles of $A_{R,i}$ and $A_{M,i}$ for the range of data from $i = 0$ to $i = n - k - 5$. Because the number of images available decrease with Δt, the above procedure ensures that at least five images are included in the estimates of $\overline{A_{R,i}}$ and $\overline{A_{M,i}}$ at every Δt (Figures 3g and 3h). The best-fit equations to data provide estimates of the mobility parameters C_R, P_R, C_M, and P_M for each quantile (25th, 50th, and 75th), which quantify the uncertainty in the mobility metrics for each river reach.

3.2.3. Examples of River Mobility Measurement Using the Landsat Archive

We show applications of our area-based mobility framework to three types of natural river systems. We chose canonical examples covering meandering rivers, braided rivers, and a river avulsion to highlight the broad

applicability of our framework. We use the Trinity River, USA, as a case-example because it is an exceptionally studied meandering river with constrained bank migration rates (Mason & Mohrig, 2018, 2019; Wellmeyer et al., 2005). Specifically, we use a ~13.5 km reach of the Trinity River near Liberty, TX (Figure 1), which encompasses 20 channel bends resulting in a 98 km² study area (see Movie S4). At this location, the Trinity River is roughly 100 m wide with a reach-averaged centerline migration rate of 2.8 m/yr (Wellmeyer et al., 2005).

To supplement the detailed case example from the Trinity River, we also calculated area-based mobilities for an additional 14 meandering rivers for which we have paired measurements centerline migration rates and channel-bend cutoff frequencies (Figure 1). We measured the suite of mobility parameters for reach areas encompassing 10–20 channel bends following methods outlined in Sections 3.2.1 and 3.2.2. We chose specific locations for meandering rivers where we also have measurements of channel centerline migration rates, M_r, and channel width, B. Centerline migration rates, were derived from a dynamic-time warping technique of channel centerlines (Sylvester et al., 2019) from paired binary channel masks between 1990 and 2020 (Greenberg & Ganti, 2021). Channel-bend cutoff frequencies were measured as the total number of cutoff-events between 1985 and 2021. Data locations, mobility measurements, and data sources are summarized in Table S2 in Supporting Information S1. Input channel masks from which we measured area-based mobility, centerline migration rates, and channel-bend cutoff frequencies are provided in the full data repository.

The South Saskatchewan River, CA, near Outlook, CA, is a canonical braided river reach and is one of the few locations with measured mid-channel bar migration rates (Strick et al., 2019). Additionally, there is significant variation in the confinement of the channel from highly confined within a valley upstream near Outlook, CA, to a wide floodplain downstream near Saskatoon, CA. This allows us to explore if the area-based mobility metrics are sensitive to observable changes in the confinement and qualitative mobility style of the South Saskatchewan River. We compare the area-based mobility of an 85.7 km² reach in the confined portion of the South Saskatchewan near Outlook, CA (51.59, −107.02) (see Movie S5) to a 107.5 km² reach of the more sinuous section of the river near Saskatchewan, CA (51.89, −106.76). This provides a comparison of area-based mobility between multi-threaded rivers with different sinuosity values.

Finally, we also present an application of our area-based mobility metrics to a natural fan-scale avulsion with a focus on a 324 km² fluvial surface area of the Beki River, India (see Movie S6). After 2001, the Beki River began to avulse, completing a near complete transfer of flow by 2006 (Sah & Das, 2018). With applications to meandering rivers, a braided river, and an avulsing river, we directly compare the estimated area-based mobility parameters across all rivers presented in this study. We explore how the two parameter spaces, that is, T_R versus A_R^* and T_M versus A_M^*, as well as the resulting R and M vary across systems and the dominant processes active therein.

4. Results

4.1. Mobility Results From Application to Numerical Models

Our area-based framework captures the trends in mobility forced in the meandering river and the fan-scale avulsion models. We find that the exponential functions (Equations 2 and 5) accurately capture the growth and decay in floodplain reworking and channel overlap decay, respectively, across all migration constants, kl, in the meandering river model (Figures 4a and 4b). With increasing values of kl, we find that the normalized active floodplain area, A_R^*, increases. This trend correlates with longer values of the reworking timescale, T_R (Figure 4c; Spearman's rank correlation coefficient, $\rho = 1.0$; P-value < 10-10), indicating that the fastest migrating simulated rivers are associated with the largest estimated active floodplain area, and the longest reworking timescale. The estimated linear reworking constant, R, values are also positively correlated with the migration constant ($\rho = 0.86$; P-value = 0.006; Figure 4d). Similarly, as the normalized long-term decay area, A_M^*, increases, the overlap decay timescale, T_M, decreases (Figure 4e; $\rho = -0.38$; P-value = 0.35), which results in a positive correlation between the linear overlap decay constant, M, and kl ($\rho = 0.86$; P-value = 0.006; Figure 4f). This observation indicates that the fastest migrating simulated rivers reorganize such that they lose nearly complete overlap in their wetted area over relatively short timescales.

We find that Equations 2 and 5 accurately describe the data derived from the meandering river model when varying cutoff thresholds, cl (Figures 4g and 4h). With varying cl, both A_R^* and T_R increase (Figure 4i; $\rho = 0.95$; P-value = 2×10^{-5}), and cl and R are positively correlated (Figure 4j; $\rho = 0.82$; P-value = 0.004). The normalized active floodplain area is positively correlated with cutoff threshold; however, A_R^* is less sensitive to changes in
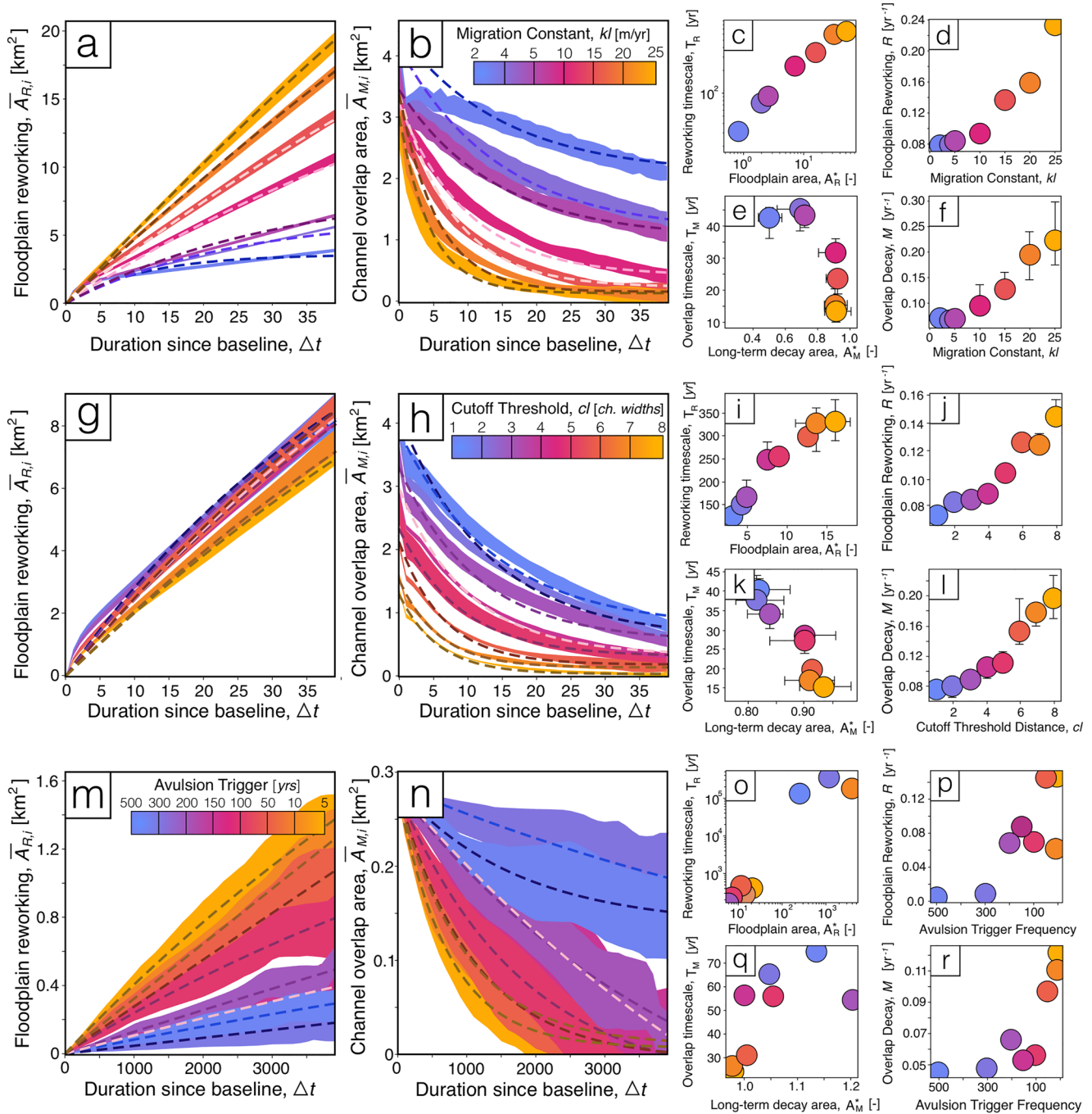
Figure 4. *Numerical modeling results of channel migration, bend-cutoff, and fan-scale avulsion.* Exponential growth and decay in (a) $\overline{A_{R,i}}$ and (b) $\overline{A_{M,i}}$ with varying kl, respectively. Colors indicate model runs with varying kl with the median (dotted lines) and IQR (shaded region) trajectories. Functional dependence of (c) A_R^* and T_R with different kl, (d) R and kl, (e) A_M^* and T_M for different kl, (f) M and kl for all the meandering model runs with varying migration constant. Exponential growth and decay in (g) $\overline{A_{R,i}}$ and (h) $\overline{A_{M,i}}$ for different cl, respectively. Functional dependence of (i) T_R on A_R^* for varying cl, (j) R on cl, (k) T_M on A_M^* with varying cl, and (l) M on cl. Exponential growth and decay in (m) $\overline{A_{R,i}}$ and (n) $\overline{A_{M,i}}$ for different avulsion trigger frequency, respectively. Functional dependence of (o) T_R on A_R^* with varying avulsion trigger frequency, (p) R on avulsion trigger frequency, (q) T_M on A_M^* with varying avulsion trigger frequency, and (r) M on avulsion trigger frequency.

cl when compared to the migration constant (Figure 4c). We also find that A_M^* and T_M are negatively correlated for varying cl (Figure 4k; $\rho = -0.85$; P-value $= 0.002$), and M is positively correlated with the cutoff frequency (Figure 4l; $\rho = 0.80$; P-value $= 0.005$). The simulated rivers with the most frequent cutoffs lose overlap of previous channel positions faster than simulated rivers with less frequent cutoffs, but the differences in normalized

long-term decay area are less sensitive to changes in cl, when compared to changes in kl (Figure 4i). Together, these modeling results indicate that our mobility framework accurately captures the relative rates and magnitudes of floodplain-scale processes and channel thread reorganization across varying rates of lateral migration and channel-bend cutoff. Further, linear mobility constants (R and M) provide metrics to compare across rivers.

For the avulsion model results, we found that Equations 2 and 5 describe the floodplain reworking and the channel overlap decay terms (Figures 4m and 4n). We find positive correlation between T_R and A_R^* (Figure 4o; $\rho = 0.86$; P-value = 0.013), and a negative correlation between the avulsion trigger frequency and R (Figure 4p; $\rho = -0.75$; P-value = 0.052). These results suggest that more frequent avulsions result in either a larger active floodplain area or a faster rate to rework the active floodplain area. In contrast to the meandering model results, we find a positive correlation between T_M and A_M^* (Figure 4q; $\rho = 0.79$; P-value = 0.036). For larger avulsion trigger periods, the decay in $\overline{A_{M,i}}$ often appears linear and results in negative estimated P_R values as the exponential attempts to mimic a linear function (Figure 4n). We find a negative correlation between the avulsion trigger frequency and M (Figure 4r; $\rho = -1.0$; P-value $< 10^{-10}$), suggesting that more frequent avulsions result in a higher M value. Together, these results indicate that the mobility framework can describe the frequency and spatial character of river avulsions, and that linear mobility constants are sensitive to this specific mobility process.

4.2. Mobility Results From Application to Remotely Sensed Rivers

4.2.1. Results From Application of the Mobility Framework to Meandering Rivers

Results indicate that the mobility metrics successfully quantify the rates of morphodynamic processes in natural meandering rivers (Figure 5). For the Trinity River, we find that $\overline{A_w}$ is 1.94 ± 0.03 km^2 (mean and standard error) averaged across the 37 years of annual composite imagery (Figure 5a). Qualitatively, the time series of channel masks depict gradual single-thread migration, including a channel bend cutoff at the northern end of the reach (Figure 5b). Equation 2 describes the exponential growth in $\overline{A_{R,i}}$ for the 25th ($R^2 = 0.98$), 50th ($R^2 = 0.99$), and 75th percentiles ($R^2 = 0.97$). The estimated C_R ranged between [0.012, 0.093] yr^{-1} with a median of 0.057 yr^{-1}, and the estimated $P_R \in [2.54, 7.01]$ km^2 with a median of 2.80 km^2. We estimated a normalized floodplain area of $A_R^* \in [1.31, 3.61]$ with a median of 1.44 and floodplain reworking timescale of $T_R \in [32.3, 250]$ yr with a median of 52.6 yr. The estimated $R \in [0.044, 0.122]$ yr^{-1} with a median $R = 0.082$ yr^{-1}.

The channel overlap decay describes the decay in $\overline{A_{M,i}}$ (Equation 4) across the 25th ($R^2 = 0.66$), 50th ($R^2 = 0.93$), and 75th percentiles ($R^2 = 0.92$). The estimated $C_M \in [0.021, 0.292]$yr^{-1} with a median 0.087 yr^{-1} and $P_M \in [-0.045, 0.888]$ km^2 with a median of 0.856 km^2, which corresponds to a normalized long-term decay area of $A_M^* \in [0.542, 1.02]$ with a median of 0.559. The channel overlap decay timescale is $T_M \in [10.3, 142.9]$ yr with a median of 34.5 yr. The measured channel overlap decay constant is $M \in [0.021, 0.158]$yr^{-1} with a median 0.049 yr^{-1}.

We also find that the floodplain reworking constant and channel overlap decay constant are consistent with the estimated migration rates of the Trinity River derived from centerline-based methods. A published migration rate of 2.8 m/yr (Wellmeyer et al., 2005) corresponds to a width-normalized migration rate of 0.028 yr^{-1}, which is comparable to the linear rate constants, R and M, estimated from channel mask time series.

Results also reveal that R and M are correlated to independent measurements of river mobility in 15 natural meandering rivers. Both the linear floodplain reworking constant (Equation 3) and the linear channel overlap decay constant (Equation 6) correlate to width-normalized migration rates, calculated as the reach-averaged centerline migration rate, M_r, divided by the reach-averaged channel width, B (Figures 5e and 5f). The spearman rank correlation coefficients between R and $\frac{M_r}{B}$ and M and $\frac{M_r}{B}$ are $\rho = 0.6$ (P-value = 0.023) and $\rho = 0.55$ (P-value = 0.43), respectively. The estimated R and M are also associated with the number of channel-bend cutoffs in each of these 15 rivers (Figures 5g and 5h). The spearman rank correlation coefficients between the number of cutoffs and R and M are $\rho = 0.66$ (P-value = 0.010) and $\rho = 0.63$ (P-value = 0.015), respectively. Together, these results indicate that the mobility metrics capture trends in both gradual migration rates and channel cutoff frequency across a diverse set of meandering rivers.

4.2.2. Results From Application of the Mobility Framework to a Braided River

Results from the application of the mobility framework to the South Saskatchewan River demonstrate that area-based mobility metrics successfully capture variations in mobility in a braided river (Figure 6). We examine
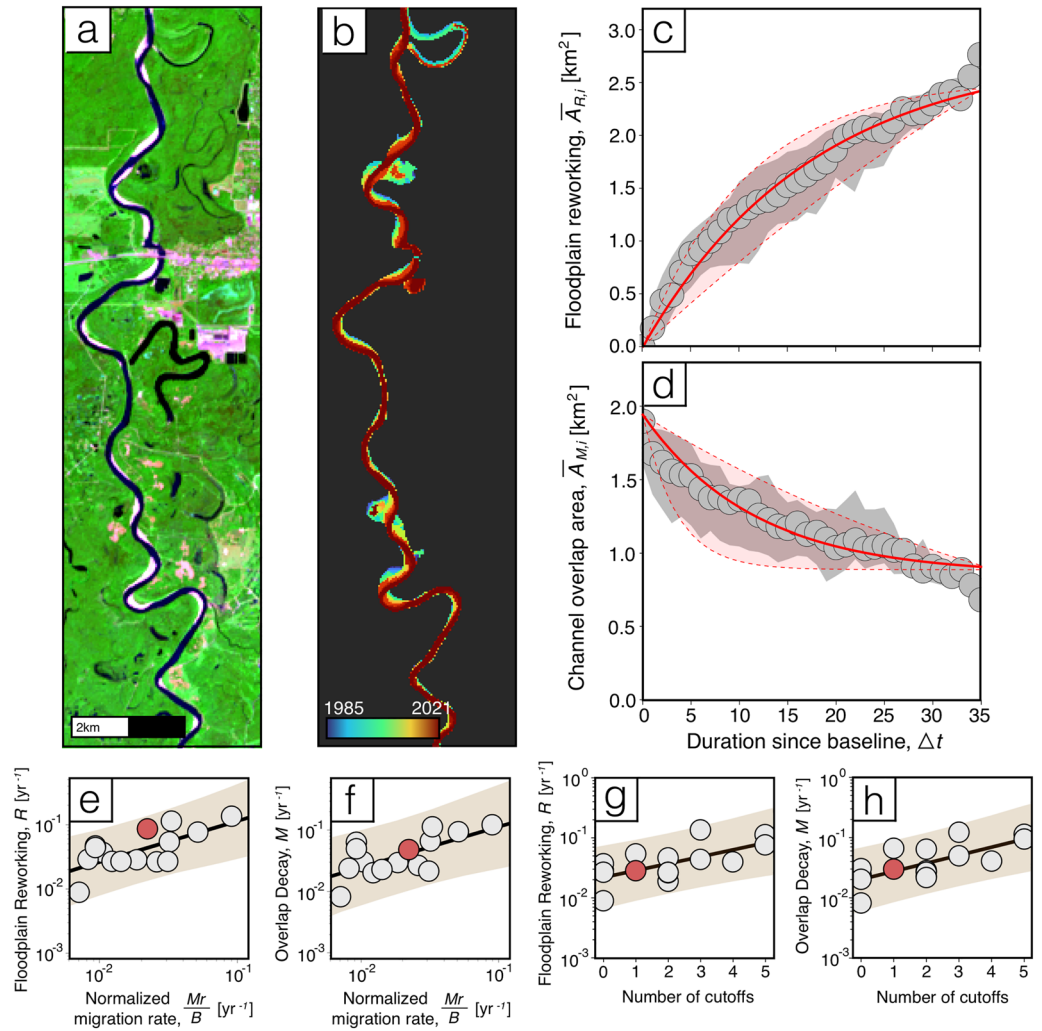
Figure 5. *Detailed application of mobility framework to meandering rivers*. (a) 2021 Landsat image (SWIR, NIR, Green) of the Trinity River near Liberty, TX. (b) Stacked channel masks using the conservative partial surface water Dynamic Surface Water Extent threshold, showing the gradual migration over the length of the reach. A cutoff occurred in the northernmost bend. (c) Exponential growth in $\overline{A_{R,i}}$ and (d) exponential decay in $\overline{A_{M,i}}$ for the Trinity River reach. Gray circles and shaded area denote the median and IQR of the variable for a given Δt, respectively. The solid and dashed red lines denote the best-fit exponential function (Equation 2 or Equation 5) for the median trajectory and the 25th and 75th percentile trajectories, respectively. Relation between centerline migration rate, M_r, normalized by channel width, B, and (e) R and (f) $^{M_r}/_B$ and M for 15 meandering rivers (red dot indicates Trinity River). Dependence of the number of cutoffs observed in the Landsat archive on (g) R and (h) M.

a confined reach near Outlook, CA (Figure 6b) and a sinuous reach near Saskatoon, CA (Figure 6c). Near Outlook, CA, the river is laterally restricted to a 500 m wide channel belt with a water depth <2 m (Strick et al., 2019). From 1985 to 2021, most of the channel-belt experienced fluvial activity—only a few bars remained dry (Figure 6b). We measured $\overline{A_w} = 7.3 \pm 0.09$ km^2, which for a downstream reach length of approximately 17.3 km, corresponds to a measured wetted area width of 422 m. The floodplain reworking and the channel overlap decay are characterized by exponential growth and decay, respectively (Figures 6d and 6e), across the 25th ($R^2 = 0.95$ for $\overline{A_{R,i}}$ and $R^2 = 0.80$ for $\overline{A_{M,i}}$), 50th ($R^2 = 0.96$ and $R^2 = 0.62$), and 75th percentiles ($R^2 = 0.93$ and $R^2 = 0.51$). Compared to the Trinity River, however, the trajectory of these curves is more variable between different baselines, which produces a wider interquartile range in $\overline{A_{R,i}}$ and $\overline{A_{M,i}}$ for a given Δt. We estimate $C_R \in [0.22, 0.44]$ yr^{-1} with a median 0.20 yr^{-1} and $P_R \in [1.8, 5.8]$ km^2 with a median of 3.1 km^2. This corresponds to $A_R^* \in [0.31, 0.65]$ with a median of 0.42, floodplain reworking timescale of $T_R \in [6.9, 15.3]$ yr with a median 13.5 yr, and a linear floodplain reworking constant of $R \in [0.07, 0.28]$ yr^{-1} with a median 0.08 yr^{-1}. We estimate $C_M \in [0.20, 3.5]$ yr^{-1}
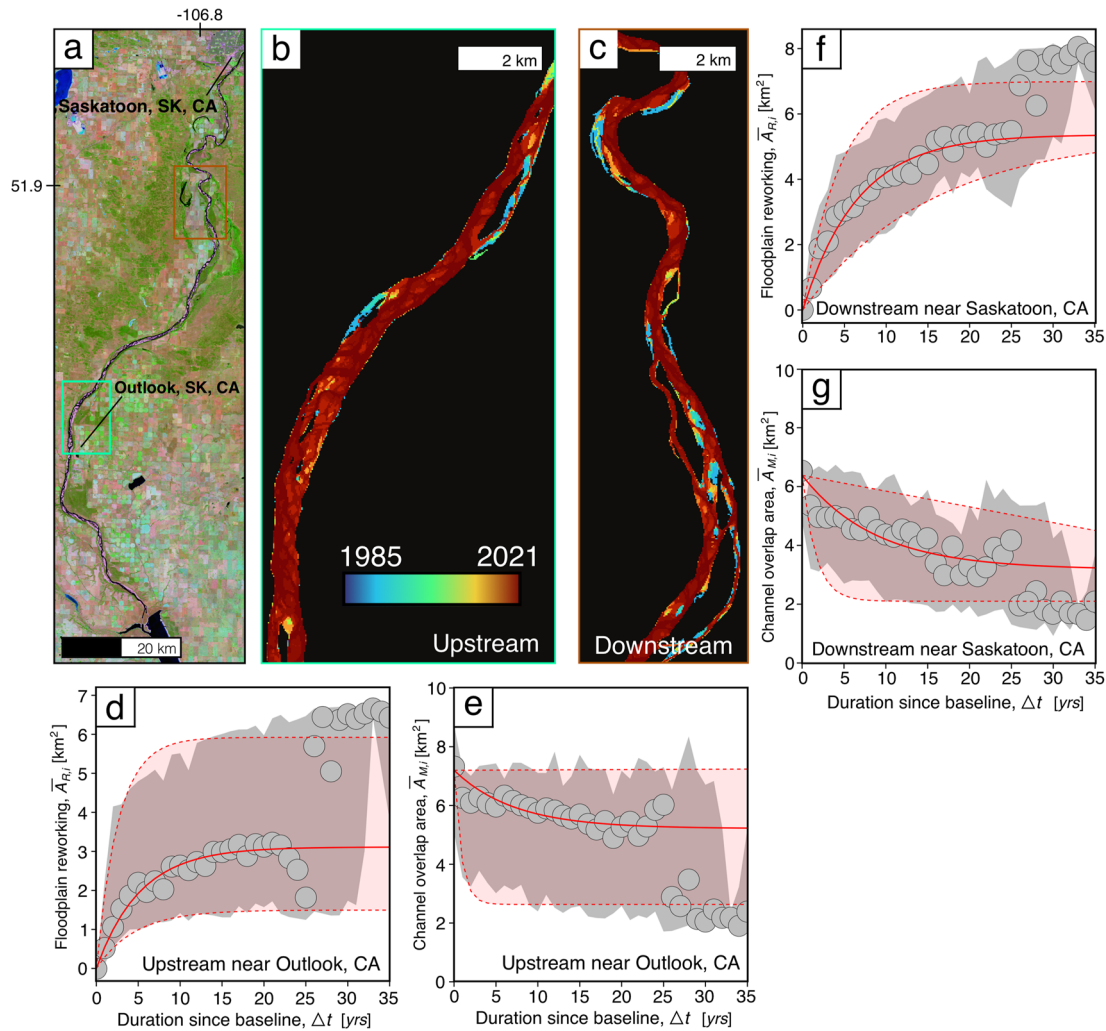
Figure 6. *Detailed application to a braided river*. (a) 2021 Landsat image (SWIR, NIR, Green) of the South Saskatchewan River from the Gardiner Dam to Saskatoon, SK, CA. The examined upstream (green) and downstream (red) reaches are boxed. (b) Stacked channel masks using the conservative partial surface water Dynamic Surface Water Extent threshold of the upstream section near Outlook, CA. This image shows that the river activity is confined within a narrow channel-belt. (c) Stacked channel masks of the downstream section near Saskatoon, CA. Channel activity is more sinuous and significantly less confined. We show the (d) growth in $\overline{A_{R,i}}$ and (e) decay in $\overline{A_{M,i}}$ for the downstream reach near Saskatoon, CA. Gray circles and shaded region indicate the median and IQR trajectory of the variable with respect to Δt, respectively. We show the (f) growth in $\overline{A_{R,i}}$ and (e) decay in $\overline{A_{M,i}}$ for the upstream reach near Outlook, CA.

with a median 0.23 yr^{-1} and $P_M \in [2.3, 7.2]$ km^2 with a median of 5.5 km^2. This results in a long-term overlap decay area of $A_M^* \in [0.19, 0.51]$ with a median of 0.25, an overlap decay timescale, $T_M \in [0.86, 14.6]$ yr with a median 13.0 yr, and a linear channel overlap decay constant of $M \in [0.06, 0.65]$ yr^{-1} with a median 0.10 yr^{-1}. Strick et al. (2019) measure a median unit bar migration rate of 175.2 $^m/_{yr}$, which is equivalent to a normalized bar migration timescale, $\frac{Mr}{B} \approx 0.415$ yr^{-1}, assuming that the downstream length of channel bars is proportional to their width (Holzweber et al., 2014). This estimate overlaps with the upper percentiles of the measured linear mobility constants.

We also calculate the mobility metrics in a less confined reach of the South Saskatchewan River near Saskatoon, CA (Figure 6c). We measure $\overline{A_w} = 6.2 \pm 0.02$ km^2 for the 23.8 km reach. For the floodplain reworking metrics, we find $C_R \in [0.04, 0.24]$ yr^{-1} with a median 0.15 yr^{-1} and $P_R \in [5.3, 7.4]$ km^2 with a median of 6.8 km^2, and corresponds to $R \in [0.08, 0.21]$ yr^{-1} with a median 0.13 yr^{-1}. For the overlap decay metrics, we estimate $C_M \in [0.07, 0.19]$ yr^{-1} with a median 0.08 yr^{-1}, $P_M \in [1.8, 4.2]$ km^2 with a median of 2.6 km^2, and $M \in [0.04, 0.12]$ yr^{-1} with a median 0.05 yr^{-1}. The less confined downstream reach has a slower M, but faster R, which is a result of the larger estimated active floodplain area.
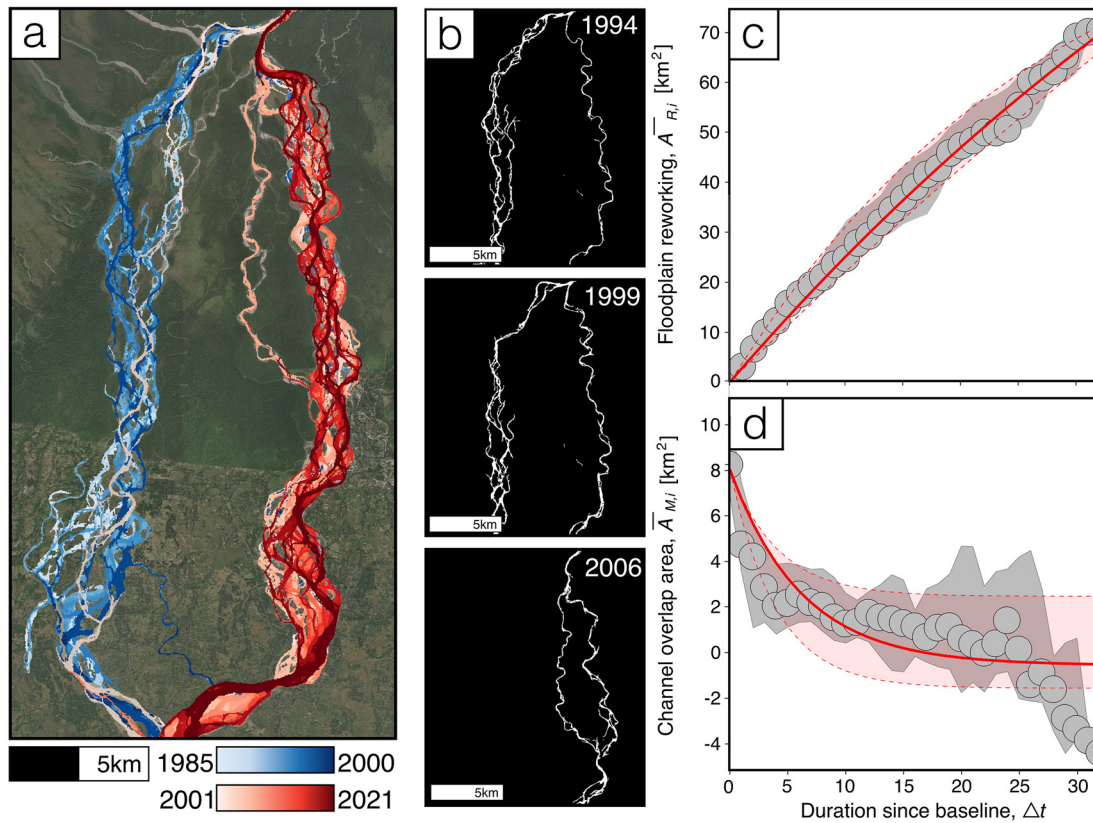
Figure 7. *Detailed application of mobility framework to a river avulsion*. (a) Stacked channel mask positions of the Beki River, India, showing the avulsion in 2001. Blue and red masks (using conservative partial surface water Dynamic Surface Water Extent threshold) are the channel locations pre-2001 and post-2001, respectively. (b) Three binary channel masks showing the differences in channel position between 1994 and 2006. (c) Exponential growth in $\overline{A_{R,i}}$ and (d) exponential decay in $\overline{A_{M,i}}$ for the Beki River fan. Gray circles and shaded area denote the median and IQR of the variable with respect to Δt, respectively. The solid and dotted red lines denote the best fit exponential functions (Equation 2 or Equation 5) to the median, and 25th and 75th percentile trajectories, respectively.

4.2.3. Results From Application of the Mobility Framework to River Avulsion

The area-based mobility metrics also successfully quantify river mobility at the fan-scale, integrating both channel-thread and channel-avulsion processes. The time series of channel masks for the Beki River reveal that a major river avulsion occurred in 2001, with the western channel belt receiving most of the flow from 1985 to 2000 and the eastern channel belt capturing most of the flow from 2001 to 2021 (Figures 7a and 7b). Across this period, we measure $\overline{A_w} = 7.84 \pm 3.7\,\text{km}^2$. Floodplain reworking term is well-characterized by the exponential growth (Equation 2) across the 25th ($R^2 = 0.99$), 50th ($R^2 = 0.99$), and 75th ($R^2 = 0.99$) percentiles. Similarly, channel overlap decay term is characterized by exponential decay (Equation 5) at 25th ($R^2 = 0.71$), 50th ($R^2 = 0.73$), and 75th ($R^2 = 0.68$) percentiles. The estimated parameters from Equation 2 are $C_R \in [0.006, 0.035]\,\text{yr}^{-1}$ (median of $0.014\,\text{yr}^{-1}$) and $P_R \in [105.6, 366.5]\,\text{km}^2$ (median of $197.6\,\text{km}^2$). This corresponds to $A_R^* \in [8.0, 52.6]$ (median of 18.8), $T_R \in [77.0, 394.9.0]\,\text{yr}$ (median of 164.2 yr), and a linear floodplain reworking rate of $R \in [0.313, 0.399]\,\text{yr}^{-1}$ (median $0.344\,\text{yr}^{-1}$). Similarly, the estimated parameters from the characterization of the channel-overlap decay term are $C_M \in [0.162, 0.253]\,\text{yr}^{-1}$ (median of $0.242\,\text{yr}^{-1}$) and $P_M \in [-1.56, 2.48]\,\text{km}^2$ (median of $-0.552\,\text{km}^2$). The negative value in estimated P_M captures the fact that more pixels have switched state from wet-to-dry or vice versa before and after an avulsion than the total number of wet pixels in a baseline image (i.e., $D_i > A_w$ in Equation 4). The corresponding mobility metrics are $A_M^* \in [0.74, 1.32]$ (median of 0.95) and $T_M \in [5.5, 22.4]\,\text{yr}$ (median of 12.2 yr). The resulting linear channel overlap decay constant is $M \in [0.178, 0.404]\,\text{yr}^{-1}$ with a median $0.235\,\text{yr}^{-1}$. Together, these results indicate that area-based mobility metrics can quantify fan-scale avulsion processes.

4.2.4. Comparison of Mobility Metrics Across River Planform and Mobility Processes

We directly compare mobility metrics across the rivers presented in previous subsections (Figure 8). The active floodplain size normalized by wetted area, A_R^*, and the reworking timescale, T_R, are positively correlated across
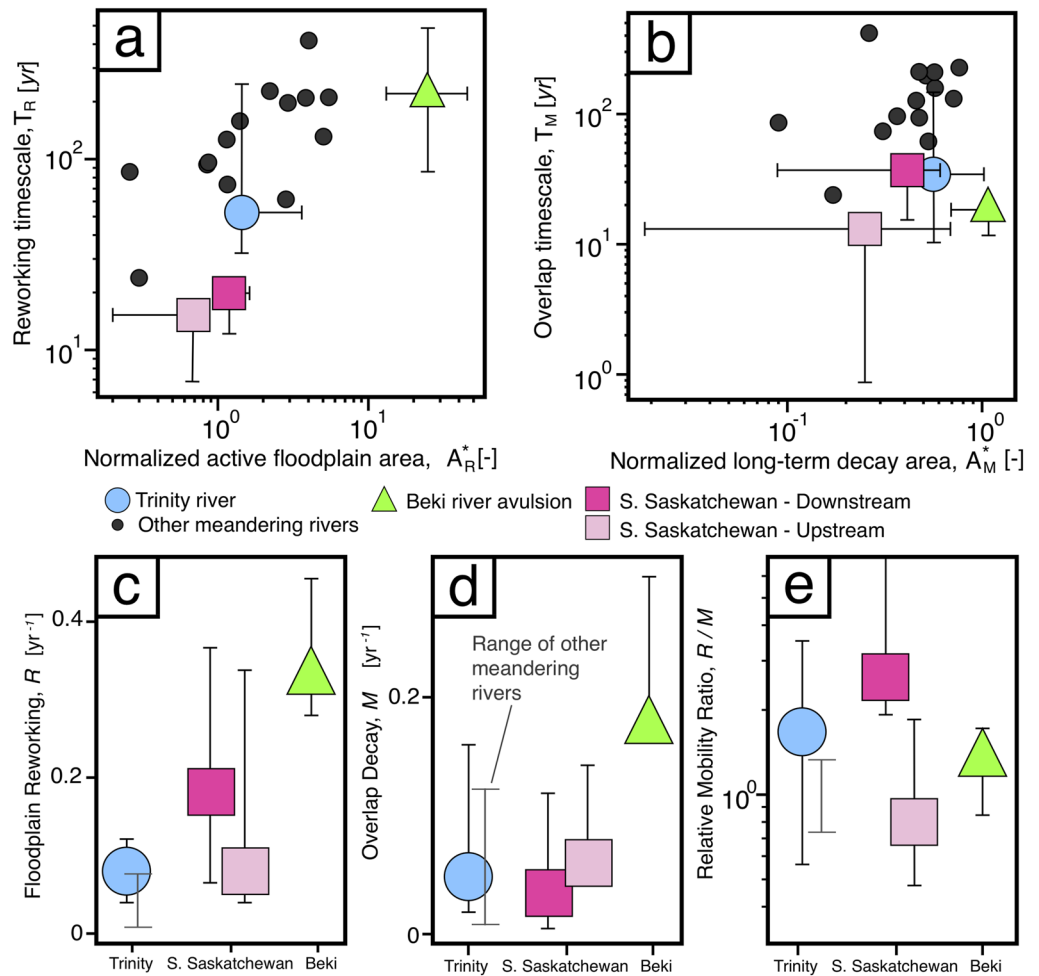
Figure 8. *Comparing mobility across river examples.* (a) Comparison of the floodplain area and reworking timescale across all rivers. Brown, blue, and green circles are the upstream (light) and downstream (dark) portions of the braided South Saskatchewan River, the meandering Trinity River, and the avulsing Beki River, respectively. Small black circles are the 14 additional meandering rivers. (b) Comparison of the long-term decay area and the overlap decay timescale across rivers. Direct comparison of the (c) linear floodplain reworking rate constants, linear channel overlap decay rate, and (e) the relative mobility ratio, *M/R*, across different rivers. Whiskers show the interquartile range of the estimated mobility parameters.

all processes and planforms (Figure 8a; $\rho = 0.77$, *P*-value = 0.00006). The Beki River avulsion has the largest normalized floodplain size ($A_R^* = 24.6$) and the slowest floodplain reworking timescale (214 yr), while the confined upstream reach of the South Saskatchewan River has both a small normalized floodplain size ($A_R^* = 0.42$) and the fastest floodplain reworking timescale (15 yr). The P_R value for the Beki River corresponds to the scale of a fluvial fan, while the P_R value for the South Saskatchewan River corresponds to the scale of the channel belt. Consequently, the small, normalized floodplain area and fast reworking timescale for the South Saskatchewan River compared to the large, normalized floodplain area and slow reworking timescale for the Beki River suggests that the primary means for braided rivers to access significant floodplain areas is through avulsions, rather than the gradual lateral migration present in the meandering river data. Results indicate that the linear floodplain reworking constant, *R*, for the Beki River is different than the meandering and braided channels (Figure 8c). A large *R* value for Beki River avulsion (0.34 yr^{-1}) suggests that the system reworks its channel-belt quickly (214 yr) relative to its large channel-belt size. This observation is physically intuitive because a river avulsion accesses a floodplain area at the spatial scale of a fluvial fan in a short period of time.

The long-term decay area normalized by the wetted area, A_M^*, and the overlap decay timescale, T_M, are not positively correlated (Figure 8b; $\rho = 0.233$, *P*-value = 0.322). The upstream braided reach of the South Saskatchewan River has a small A_M^* value of 0.25 and fast T_M (16 yr), which suggests that the South Saskatchewan River has

fast thread-scale dynamics, but threads consistently return to the same area. The linear overlap decay constants, M, are comparable between the upstream portion of the South Saskatchewan River (0.1 yr^{-1}) and Beki River avulsion (0.23 yr^{-1}), The change in sinuosity in the South Saskatchewan River corresponds to differences in M, where M is lower for the sinuous downstream reach (0.05)—a comparable rate to the meandering rivers (Figure 8d). Finally, the relative mobility ratio, R/M, captures potential differences in processes between the two metrics. The upstream braided reach of the South Saskatchewan River has a lower relative mobility ratio (0.8) when compared to the downstream South Saskatchewan River reach (2.6), the Trinity River (1.7), and the Beki River avulsion (1.4) (Figure 8e). These values indicate that for the confined braided South Saskatchewan River, the rate at which river threads evolve significantly outpaces the rate at which the channel-belt grows—intuitive for a laterally confined river.

5. Sensitivity Analysis

Our results indicate that area-based mobility metrics provide a quantitative framework to compare river mobility across different rivers from satellite imagery (Figures 4–8). In this section, we quantify the sensitivity of these metrics to the types of natural variability in application and data quality. Quantifying the effect of natural variability is important when comparing measurements from one river to another, which includes differences in the size of the fluvial surface, the observation length, errors of omission and commission in the water masks, and natural stage variation within the channel mask time series. Unfavorable effects from inconsistencies in the surrounding factors of application could lead to inaccurate results and confound potential signals. We explore how each of these potential effects influences the resulting mobility metrics and provide heuristics to guide application.

5.1. Effect of Fluvial Surface Area

Measuring area-based mobility in different rivers of varying size will necessitate using different fluvial surface areas to calculate the floodplain reworking and channel overlap decay metrics. One critical advantage in applying an area-based framework to experimental rivers is that the fluvial surface area is carefully controlled, and the river migrates over the entire fluvial surface during the experiment. In natural rivers, the apparent fluvial surface—the area over which there are both active indicators and landform relics (e.g., oxbow lakes)—is often much larger than the area the river will access over the time-extent of remote imagery. To assess if the extent of the fluvial surface area affects the measured mobility metrics, we considered an arbitrary 17-by-17-km area of the Brahmaputra River, India, and calculated R and M for the reach while varying the size of the fluvial surface by changing the extent of the observation area (Figure 9a). Our sensitivity analysis revealed that the estimated R and M are invariant with the fluvial surface area size, which is in contrast to the original formulation of Wickert et al. (2013) (Figure S3 in Supporting Information S1). Thus, the extent of the fluvial surface area used to calculate the area-based mobility is not a critical concern when applying our mobility framework.

5.2. Effect of Observation Duration

While the observation duration is roughly similar across Landsat applications (~37 years), the time captured relative to the rate of river mobility will vary across rivers. We show the effect of variable observation duration relative to river mobility by examining how calculated mobility metrics change for a 42 km^2 fluvial surface of the Rio Bermejo, AR (−24.63, −61.26) with varying observation duration (Figure 9b). We computed mobility metrics over varying observation duration, where 10 years indicates the period 1987–1997, 20 years indicates the period 1987–2007, and so forth. Our sensitivity analysis revealed that R and M vary as a function of observation duration, but the estimated rate constants correlate with the measured centerline migration rates for the same reach. Short observation durations that only capture the early fast migration history of the Rio Bermejo are higher than metrics that include the entire 37-year history, which capture both the period of fast centerline migration and slower centerline migration after 2000. Our sensitivity analysis revealed that the estimated mobility is less reliable when rivers migrate less than one channel area during the observation duration (Figure S4 in Supporting Information S1). Thus, estimated mobility may be susceptible to bias for rivers with very slow mobility rates or for rivers with limited observation duration.

5.3. Effect of Classification Accuracy and River Stage Variation

The accuracy of river classification and river stage variation are distinct sources of uncertainty in the channel masks, which form the underlying data of our mobility framework. While annual composites eliminate some
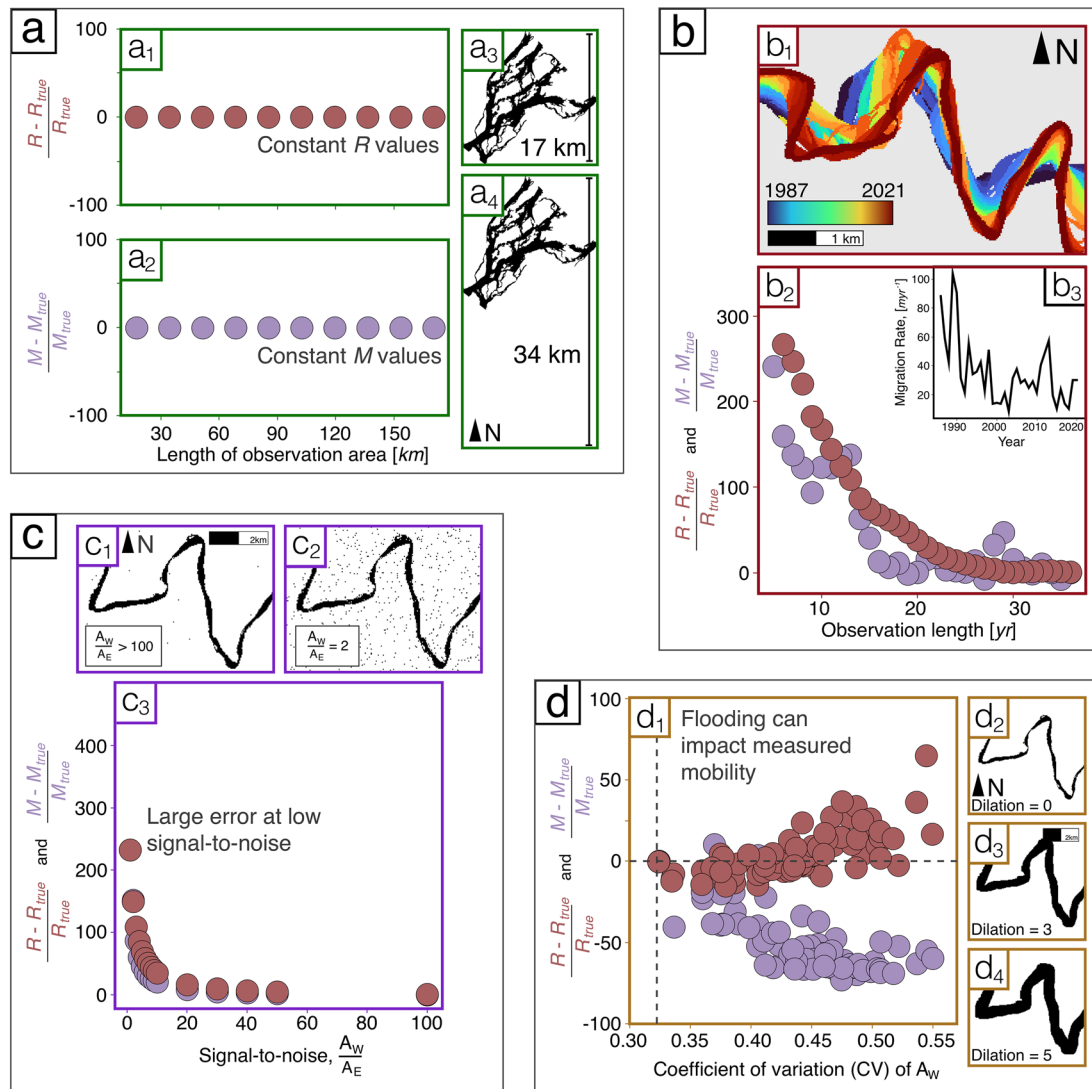
Figure 9. *Results from sensitivity analyses*. (a) Effect of varying fluvial surface area on mobility metrics. (a$_1$ and a$_2$) Our metrics are insensitive to variations in the size of the observation area. (a$_3$ and a$_4$) We varied channel-mask area by adjusting the size of the input channel masks from the Brahmaputra River (27.4686, 94.8130). Sensitivity is reported as percent relative to a value of R_{true} and M_{true} measured from a mask height of 17 km. (b) Effect of observation duration on mobility metrics. (b$_1$) Stacked channel mask locations of the Rio Bermejo, AR, from 1987 to 2021 (−61.2561, −24.6340). (b$_2$) The change in measured R and M relative to an assumed Landsat-average value taken as the mobility measured using a 37-year observation duration (R_{true} and M_{true}). (b$_3$) The reach-averaged centerline migration rate for the same reach. (c) Effect of pixel misclassification on mobility metrics. Top images show binary channel masks of the Rio Bermejo, AR, with low (c$_1$) and high (c$_2$) signal-to-noise ratios. (c$_3$) The change in measured R and M while increasing the signal-to-noise relative to an assumed "true" value calculated with no added-noise (R_{true} and M_{true}). (d) Effect of river stage variation on calculated metrics. (d$_1$) Differences in calculated R and M with varying CV(A_w) relative to values calculated with no simulated flooding. The vertical dotted line is the coefficient of variation of the "true" data with no simulated flooding. We show simulated data with (d$_2$) no flooding (R_{true} and M_{true}), (d$_3$) intermediate flooding, and (d$_4$) high flooding. Binary dilations grow the water pixels by adjacency, and multiple passes increase the water area.

of the variability in data quality from one image to another (Schwenk et al., 2017), the quality of composite images can vary from one year to another and lead to differences in classification accuracy. Further, annual composite-derived channel masks also capture variability arising from river stage. Interannual variability in river discharge, and subsequently stage, will be expressed as variability in wetted river area in annual channel masks. Consequently, both the errors of omission and commission in channel mask classification and interannual stage variability constitute noise; pixel water surface changes that are not a function of river mobility, but will be erroneously incorporated into mobility calculations (Langhorst & Pavelsky, 2023). The relative signal-to-noise ratio of the channel masks arising from differences in classification accuracy and river stage variation can significantly influence the river mobility metrics. To assess the consequences of channel mask noise in the calculation of area-based mobility metrics, we performed two experiments. First, we examined how errors of omission and

commission and mis-classified pixels affect estimated rate constants. Second, we examined how interannual variations in river stage can impact resulting mobility calculations.

We designed an experiment on the same time series of natural channel masks from Rio Bermejo, AR (Section 5.2), to assess how errors of omission and commission impact mobility metrics. We simulated mis-classification errors by flipping binary raster pixels (1 → 0 and 0 → 1) at random spatial pattern across the raster channel mask, which created masks with incorrectly classified channel water within the fluvial surface. We define a signal-to-noise ratio as SNR = A_W/A_E, where A_E is the area of mis-classified binary pixels. We then estimated R and M for different values of *SNR* (Figure 9c), where SNR = 100 indicates that 1 out of every 100 wetted pixels is mis-classified and SNR = 1 indicates an equal number of mis-classified pixels as wetted channel pixels. Results indicate that the estimated rate constants deviate nonlinearly from their true values for SNR < 10 (Figure 9c). At higher SNR, the two area-based mobility rates approach the true value. For applications to natural data, this suggests that if >10% of the channel area is mis-classified, the resulting R and M will misrepresent the true mobility rates. A ∼90% accuracy is a reasonable goal in the DSWE classification and river channel extraction (Jones, 2019), indicating that errors in omission and commission are unlikely to significantly affect the computation of area-based mobility metrics, which is in contrast to linear rates of river mobility computed at the bank scale (Langhorst & Pavelsky, 2023).

Interannual variability in stage height can also lead to differences in measured mobility. Varying flood stage within the annual channel masks leads to increased variability in A_w that is not a function of river mobility, just flood-driven variations in river wetted width. While interannual flooding is an important hydrological phenomenon, for this analysis, we do not attribute flood-driven changes in wetted area as river mobility. To demonstrate the effect of flood-driven variability in A_w, we provide a test showing the effect of simulated flooding on a natural channel mask time series of the same 42 km² fluvial surface of the Rio Bermejo, AR (−24.63, −61.26). For each mask within the time series, we perform an *n*-fold binary dilation, which expands each "1" pixel such that each adjacent pixel is also a "1," and will repeat the expansion *n* times. We vary the maximum *n*-fold dilation and repeat the measurement of the area-based mobility metrics. We then track the coefficient of variation of A_w to represent the degree of interannual variability in the channel masks (Figure 8d). When CV(A_w) is similar to what is observed in the natural data set then the maximum *n*-fold dilation is small, and when CV(A_w) is greater than the natural data set then the maximum *n*-fold dilation is large. Our sensitivity analysis reveals significant variability in estimated R and M with varying CV(A_w). In the case of R, significant interannual variability can lead to misleading overestimates of the true value. In the case of M, interannual variability leads to underestimates of the true value. While we found the effect of interannual flooding to be less significant than classification errors in natural applications, flood-driven variation in A_w should be a careful consideration. Minimizing interannual variation in A_w could be achieved either by focusing on similar periods of the hydrograph from year-to-year, or by omitting years with significantly different A_w.

6. Discussion

Our results show that the area-based river mobility metrics capture known trends in the rates and occurrence of river processes in meandering and braided rivers at scales ranging from a reach to a fluvial fan. We reproduce expected trends using numerical models, which demonstrate the successful application of the framework in capturing trends in river mobility under ideal, noise-free conditions (Figure 4). The application of our framework to natural river data showed that our metrics produce physically intuitive results and capture expected trends in river mobility (Figure 5). Original experimental applications of area-based metrics were limited to experimental braided rivers (Bufe et al., 2019; Wickert et al., 2013), and here, we adapted and upscaled the framework to quantify natural river mobility from satellite data (Figures 5–7). Our area-based framework to quantify river mobility can be used to directly compare mobilities across river planforms and processes (Figure 8). A systematic survey exploring how floodplain turnover and channel overlap differ between river planforms may be important. For example, differences in area-based mobility between braided and meandering rivers could highlight important differences in floodplain turnover. Area-based metrics can also be used alongside centerline-, vector- and pixel-based methods that only quantity bank migration (Chadwick et al., 2023; Rowland et al., 2016; Sylvester et al., 2019) to tease apart relative contributions of bank-scale, reach-scale and floodplain-scale processes to floodplain erosion and planform change.

The linear floodplain reworking rate constant (R) and overlap decay rate constant (M) capture different aspects of river mobility (Figure 8). Our results reveal that R and M are similar for meandering rivers, which lose overlap of their thread morphology and access new floodplain material through the process of gradual channel migration

(Figure 8). However, significant differences in R and M values exist between meandering and braided rivers broadly (Figure 8), and even between the distinct sinuosity sections of the South Saskatchewan River (Figures 7 and 8). This observation suggests that when mobility processes grow the floodplain area during thread-scale migration, like during lateral migration, R and M should be similar. When the thread-scale process does not actively grow the floodplain area, like thread-switching in braided rivers, the values of R and M will diverge (Figure 7). Thus, the ratio of R and M quantifies the magnitude of floodplain expansion relative to the magnitude of channel thread reorganization for a given reach (Figure 8).

The area-based mobility metrics developed here provide tools to quantify differences in river dynamics in response to environmental signals as well as measure the areas and rates needed to constrain organic carbon storage in fluvial environments. Our framework requires long-observation periods relative to the river mobility (Figure 9), and is ideally suited to compare rivers evolving under different boundary conditions. Broadly, we can compare rivers of all forms globally under boundary condition variations in water discharge, sediment flux, and bed slope—variables that are proposed to dictate the types and rates of river mobility processes (Bufe et al., 2019; Constantine et al., 2014; Donovan et al., 2021; Ielpi & Lapôtre, 2020; Larsen et al., 2006; Limaye, 2020; Micheli et al., 2004; Parker, 1976; Wickert et al., 2013). The age and oxidation of organic carbon in floodplains is in part controlled by the area over which the river is active, and how often the river reworks this floodplain material (Torres et al., 2017). Our mobility framework directly quantifies the relevant rates and scales of fluvial activity. The estimated floodplain area, P_R, should correspond to the potential area for carbon storage. The reworking timescale, T_R, quantifies the typical duration for which organic carbon is allowed to age and oxidize in the floodplain (Torres et al., 2017). Our results indicate that this can be significantly different based on the dominant river mobility process and river planform (Figures 7 and 8). Within this context, meandering rivers with large, normalized floodplain areas and large long-term decay areas may access a significant area of floodplain organic carbon through lateral migration alone, but downstream transit times of fluvial organic carbon may be relatively long due to paired mobilization and deposition of organic carbon (Douglas et al., 2022; Golombek et al., 2021; Repasch et al., 2021). Alternatively, braided rivers with small normalized floodplain areas and small long-term decay areas do not access significant areas of the floodplain without avulsion processes and may isolate floodplain carbon for significant periods of time, but should have fast downstream transit times as channel-belt threads rework themselves quickly (Lininger et al., 2018).

The two primary concerns when applying our framework to remote sensing data are river mask classification accuracy and the inter-annual variability in river wetted area (Figure 9). These issues can be circumvented by targeting image acquisition from consistent periods of the hydrograph from year to year (e.g., Rowland et al., 2016). Likewise, we can minimize the effects of classification accuracy by optimizing the chosen channel mask classifier to local conditions or leveraging multiple classification strategies to propagate the uncertainty in channel mask accuracy (e.g., using multiple DSWE bands). Through sensitivity analysis, we also showed that the area-based mobility metrics are not sensitive to the size of the study area (Figure 9), and that the Landsat timespan is sufficient to quantify the channel migration of many river systems. For very slow rivers, estimates of M will be affected (Figure S4 in Supporting Information S1).

With the goal of wide applicability, we provide heuristic rules for estimating area-based mobility metrics from satellite data:

1. While there is no dependence of estimated mobility rates on observation area size, the downstream length within the defined observation area should capture the scale of river process of interest. This scale may range from a few channel bends in a meandering river to capture thread migration and channel-cutoff (Figure 5) to the scale of an entire fluvial fan to capture a major river avulsion (Figure 7).
2. The river width must be sufficiently large to ensure high signal-to-noise with respect to channel mask classification. The value of $\overline{A_w}$ is proportional to channel width and the downstream length captured in the fluvial surface area. If rivers are too narrow, then the expected errors from the mask classification will be a significant fraction of $\overline{A_w}$, such that the resulting area-based mobility is erroneously high (Figure 9). When data quality is ideal, we use a minimum threshold width of 90 m. Alternatively, commercial satellite data sets (e.g., Planet's RapidEye) offer meter-scale resolution, which could resolve mobility in smaller systems albeit over shorter timescales than Landsat data.
3. We suggest using annual composites to minimize interannual variability of $\overline{A_w}$ resulting from flood stage differences. Years with significant overbank flooding should be excluded from the analyses as these images

may bias the estimated mobility rates (Figure 9). If enough months are present in the available swath-level images, annual composites average out most of the flood stage inundation. If flooding is a persistent problem, then manual removal of flooded images may be necessary. Previous researchers also suggest using a reference discharge from periods of time that captures equivalent parts of the hydrograph (Limaye, 2017; Rowland et al., 2016; Schwenk et al., 2017). While this may further minimize interannual variability of $\overline{A_w}$, we found it to be site-dependent, which relied on detailed knowledge of local hydrographs combined with a sensitivity to availability of imagery.

4. Finally, we suggest that mobility metrics should be used to target rivers that are moving sufficiently quickly to provide accurate estimates of area-based mobility. Our results indicate that M is sensitive to the length of the observation period when rivers do not migrate close to a channel area within the observation period (Figure 9). We suggest limiting application to rivers that show mobility-related pixel change areas greater than $\overline{A_w}$.

7. Conclusions

We introduced a framework to quantify time and area-integrated metrics of river mobility from remote imagery. The framework adapts and upscales previous applications of area-based metrics designed for experimental data, and represents a first-of-its-kind application to the Landsat archive. We show that area-based metrics of river mobility are sensitive to natural river processes, including meander migration rates, channel-bend cutoff frequencies, and fan-scale river avulsion (Figures 4–7). Our framework quantifies the rates and scales of floodplain reworking and channel-thread reorganization in natural rivers across a diverse range of river planforms, and processes consistent with traditional measurements (Figures 5 and 8). Unlike traditional methods, our metrics are not designed for a specific river planform or mobility process, and thus can be applied generally to test global predictions about how rivers respond to allogenic forcings (e.g., water and sediment flux), and constrain the rates and scales of organic carbon cycling in alluvial floodplains.

Notation

i	Index for each image, unitless
k	Index for each baseline image, unitless
$A_{R,i}$, $\overline{A_{R,i}}$	Cumulative Reworked Floodplain area, km^2. Overbar indicates ensemble average.
A_d	Dry pixel area in baseline channel mask, km^2.
A_i	Cumulative unvisited floodplain pixels in first i channel masks, km^2.
P_R	Estimated active floodplain area, km^2.
C_R	Floodplain reworking growth rate, yr^{-1}.
T_R	Reworking timescale, yr.
A_R^*	Normalized active floodplain area, unitless (number of channel-areas).
R	Linear floodplain reworking constant, yr^{-1}.
$A_{M,i}$, $\overline{A_{M,i}}$	Channel overlap area, km^2. Overbar indicates ensemble average.
A_w	Wetted channel area, km^2.
D_i	Average area changed from water to dry or from dry to water, km^2.
P_M	Long-term channel area memory, km^2.
C_M	Channel overlap decay rate, yr^{-1}.
T_M	Overlap decay timescale, yr.
A_M^*	Normalized long-term decay area, unitless (number of channel-areas).
M	Linear overlap decay constant, yr^{-1}.
M_R	Centerline migration rate, m yr^{-1}.
B	Channel width, m.

Data Availability Statement

Our analysis was performed in Python 3 (Van Rossum & Drake, 1995). The codes underlying this study are publicly available in archived Zenodo repositories. To download and generate water masks from Google Earth Engine Data, visit https://doi.org/10.5281/zenodo.7747389. To apply our mobility framework, visit

https://doi.org/10.5281/zenodo.7775843. All Landsat imagery is freely available through Google Earth Engine (Gorelick et al., 2017). Code for the meandering centerline model is found at https://github.com/zsylvester/meanderpy (Sylvester et al., 2019). Code for the avulsion model is found at https://doi.org/10.5194/esurf-10-555-2022 (H. K Martin & Edmonds, 2022). To access all the underlying data used in this publication, visit https://doi.org/10.25349/D90G71.

References

Ahmed, J., Constantine, J. A., & Dunne, T. (2019). The role of sediment supply in the adjustment of channel sinuosity across the Amazon Basin. *Geology*, *47*(9), 807–810. https://doi.org/10.1130/G46319.1

Allen, G. H., & Pavelsky, T. M. (2018). Global extent of rivers and streams. *Science*, *361*(6402), 585–588. https://doi.org/10.1126/science.aat0636

Ashmore, P. (2013). Morphology and dynamics of braided rivers.

Best, J. (2019). Anthropogenic stresses on the world's big rivers. *Nature Geoscience*, *12*(1), 7–21. https://doi.org/10.1038/s41561-018-0262-x

Brooke, S. A. S., Chadwick, A. J., Silvestre, J., Lamb, M. P., Edmonds, D. A., & Ganti, V. (2022). Where rivers jump course. *Science*, *376*(6596), 987–990. https://doi.org/10.1126/science.abm1215

Brooke, S. A. S., Ganti, V., Chadwick, A. J., & Lamb, M. P. (2020). Flood variability determines the location of lobe-scale avulsions on deltas: Madagascar. *Geophysical Research Letters*, *47*(20), e2020GL088797. https://doi.org/10.1029/2020gl088797

Bryant, M., Falk, P., & Paola, C. (1995). Experimental study of avulsion frequency and rate of deposition. *Geology*, *23*(4), 365–368. https://doi.org/10.1130/0091-7613(1995)023<0365:esoafa>2.3.co;2

Bufe, A., Paola, C., & Burbank, D. W. (2016). Fluvial bevelling of topography controlled by lateral channel mobility and uplift rate. *Nature Geoscience*, *9*(9), 706–710. https://doi.org/10.1038/ngeo2773

Bufe, A., Turowski, J. M., Burbank, D. W., Paola, C., Wickert, A. D., & Tofelde, S. (2019). Controls on the lateral channel-migration rate of braided channel systems in coarse non-cohesive sediment. *Earth Surface Processes and Landforms*, *44*(14), 2823–2836. https://doi.org/10.1002/esp.4710

Cazanacli, D., Paola, C., & Parker, G. (2002). Experimental steep, braided flow: Application to flooding risk on fans. *Journal of Hydraulic Engineering*, *128*(3), 322–330. https://doi.org/10.1061/(ASCE)0733-9429(2002)128:3(322)

Chadwick, A. J., Greenberg, E., & Ganti, V. (2023). Remote sensing of riverbank migration using particle image velocimetry. *Journal of Geophysical Research: Earth Surface*, *128*(7), e2023JF007177. https://doi.org/10.1029/2023JF007177

Chadwick, A. J., Lamb, M. P., & Ganti, V. (2020). Accelerated river avulsion frequency on lowland deltas due to sea-level rise. *Proceedings of the National Academy of Sciences of the United States of Americas*, *117*(30), 17584–17590. https://doi.org/10.1073/pnas.1912351117

Chadwick, A. J., Lamb, M. P., Moodie, A. J., Parker, G., & Nittrouer, J. A. (2019). Origin of a preferential avulsion node on lowland river deltas. *Geophysical Research Letters*, *46*(8), 4267–4277. https://doi.org/10.1029/2019gl082491

Chadwick, A. J., Steele, S., Silvestre, J., & Lamb, M. P. (2022). Effect of sea-level change on river avulsions and stratigraphy for an experimental lowland delta. *Journal of Geophysical Research: Earth Surface*, *127*(7), e2021JF006422. https://doi.org/10.1029/2021jf006422

Constantine, J. A., & Dunne, T. (2008). Meander cutoff and the controls on the production of oxbow lakes. *Geology*, *36*(1), 23–26. https://doi.org/10.1130/g24130a.1

Constantine, J. A., Dunne, T., Ahmed, J., Legleiter, C., & Lazarus, E. D. (2014). Sediment supply as a driver of river meandering and floodplain evolution in the Amazon Basin. *Nature Geoscience*, *7*(12), 899–903. https://doi.org/10.1038/ngeo2282

Dethier, E. N., Renshaw, C. E., & Magilligan, F. J. (2022). Rapid changes to global river suspended sediment flux by humans. *Science*, *376*(6600), 1447–1452. https://doi.org/10.1126/science.abn7980

Dietrich, W. E., & Smith, J. D. (1983). Influence of the point bar on flow through curved channels. *Water Resources Research*, *19*(5), 1173–1192. https://doi.org/10.1029/wr019i005p01173

Donovan, M., & Belmont, P. (2019). Timescale dependence in river channel migration measurements. *Earth Surface Processes and Landforms*, *44*(8), 1530–1541. https://doi.org/10.1002/esp.4590

Donovan, M., Belmont, P., & Sylvester, Z. (2021). Evaluating the relationship between meander-bend curvature, sediment supply, and migration rates. *Journal of Geophysical Research: Earth Surface*, *126*(3), e2020JF006058. https://doi.org/10.1029/2020JF006058

Douglas, M. M., Li, G. K., Fischer, W. W., Rowland, J. C., Kemeny, P. C., West, A. J., et al. (2022). Organic carbon burial by river meandering partially offsets bank erosion carbon fluxes in a discontinuous permafrost floodplain. *Earth Surface Dynamics*, *10*(3), 421–435. https://doi.org/10.5194/esurf-10-421-2022

Finnegan, N. J., Schumer, R., & Finnegan, S. (2014). A signature of transience in bedrock river incision rates over timescales of 104–107 years. *Nature*, *505*(7483), 391–394. https://doi.org/10.1038/nature12913

Galeazzi, C., Almeida, R., & do Prado, A. (2021). Linking rivers to the rock record: Channel patterns and paleocurrent circular variance. *Geology*, *49*(11), 1402–1407. https://doi.org/10.1130/g49121.1

Ganti, V., Chadwick, A. J., Hassenruck-Gudipati, H. J., Fuller, B. M., & Lamb, M. P. (2016a). Experimental river delta size set by multiple floods and backwater hydrodynamics. *Science Advances*, *2*(5), e1501768. https://doi.org/10.1126/sciadv.1501768

Ganti, V., Chu, Z., Lamb, M. P., Nittrouer, J. A., & Parker, G. (2014). Testing morphodynamic controls on the location and frequency of river avulsions on fans versus deltas: Huanghe (Yellow River), China. *Geophysical Research Letters*, *41*(22), 7882–7890. https://doi.org/10.1002/2014GL061918

Ganti, V., Hajek, E. A., Leary, K., Straub, K. M., & Paola, C. (2020). Morphodynamic hierarchy and the fabric of the sedimentary record. *Geophysical Research Letters*, *47*(14), e2020GL087921. https://doi.org/10.1029/2020gl087921

Ganti, V., Von Hagke, C., Scherler, D., Lamb, M. P., Fischer, W. W., & Avouac, J.-P. (2016b). Time scale bias in erosion rates of glaciated landscapes. *Science Advances*, *2*(10), e1600204. https://doi.org/10.1126/sciadv.1600204

Golombek, N. Y., Scheingross, J. S., Repasch, M. N., Hovius, N., Menges, J., Sachse, D., et al. (2021). Fluvial organic carbon composition regulated by seasonal variability in lowland river migration and water discharge. *Geophysical Research Letters*, *48*(24), e2021GL093416. https://doi.org/10.1029/2021GL093416

Gorelick, N., Hancher, M., Dixon, M., Ilyushchenko, S., Thau, D., & Moore, R. (2017). Google Earth engine: Planetary-scale geospatial analysis for everyone. *Remote Sensing of Environment*, *202*, 18–27. https://doi.org/10.1016/j.rse.2017.06.031

Greenberg, E., & Ganti, V. (2021). Fluvial sediment supply controls reach-scale migration rates for meandering rivers globally, 2021, EP34A-06. In *Presented at the AGU fall meeting abstracts*.

Hajek, E. A., Paola, C., Petter, A., Alabbad, A., & Kim, W. (2014). Amplification of shoreline response to sea-level change by back-tilted subsidence. *Journal of Sedimentary Research*, *84*(6), 470–474. https://doi.org/10.2110/jsr.2014.34

Hajek, E. A., & Straub, K. M. (2017). Autogenic sedimentation in clastic stratigraphy. *Annual Review of Earth and Planetary Sciences*, *45*(1), 681–709. https://doi.org/10.1146/annurev-earth-063016-015935

Hickin, E. J., & Nanson, G. C. (1984). Lateral migration rates of river bends. *Journal of Hydraulic Engineering*, *110*(11), 1557–1567. https://doi.org/10.1061/(asce)0733-9429(1984)110:11(1557)

Holzweber, B. I., Hartley, A. J., & Weissmann, G. S. (2014). Scale invariance in fluvial barforms: Implications for interpretation of fluvial systems in the rock record. *Petroleum Geoscience*, *20*(2), 211–224. https://doi.org/10.1144/petgeo2011-056

Hooke, J. M. (2004). Cutoffs galore!: Occurrence and causes of multiple cutoffs on a meandering river. *Geomorphology*, *61*(3–4), 225–238. https://doi.org/10.1016/j.geomorph.2003.12.006

Howard, A. D., & Knutson, T. R. (1984). Sufficient conditions for river meandering: A simulation approach. *Water Resources Research*, *20*(11), 1659–1667. https://doi.org/10.1029/wr020i011p01659

Ielpi, A., & Lapôtre, M. G. (2020). A tenfold slowdown in river meander migration driven by plant life. *Nature Geoscience*, *13*(1), 82–86. https://doi.org/10.1038/s41561-019-0491-7

Ielpi, A., Lapôtre, M. G., Finotello, A., & Roy-Léveillée, P. (2023). Large sinuous rivers are slowing down in a warming Arctic. *Nature Climate Change*, *13*(4), 1–7. https://doi.org/10.1038/s41558-023-01620-9

Isikdogan, L. F., Bovik, A., & Passalacqua, P. (2017). RivaMap: An automated river analysis and mapping engine. *Remote Sensing of Environment*, *202*, 88–97. https://doi.org/10.1016/j.rse.2017.03.044

Isikdogan, L. F., Bovik, A., & Passalacqua, P. (2020). Seeing through the clouds with DeepWaterMap. *IEEE Geoscience and Remote Sensing Letters*, *17*(10), 1662–1666. https://doi.org/10.1109/LGRS.2019.2953261

Jerolmack, D. J., & Mohrig, D. (2007). Conditions for branching in depositional rivers. *Geology*, *35*(5), 463–466. https://doi.org/10.1130/g23308a.1

Jerolmack, D. J., & Swenson, J. B. (2007). Scaling relationships and evolution of distributary networks on wave-influenced deltas. *Geophysical Research Letters*, *34*(23), L23402. https://doi.org/10.1029/2007gl031823

Jones, J. W. (2019). Improved automated detection of subpixel-scale inundation—Revised dynamic surface water extent (DSWE) partial surface water tests. *Remote Sensing*, *11*(4), 374. https://doi.org/10.3390/rs11040374

Kim, W., Paola, C., Voller, V. R., & Swenson, J. B. (2006). Experimental measurement of the relative importance of controls on shoreline migration. *Journal of Sedimentary Research*, *76*(2), 270–283. https://doi.org/10.2110/jsr.2006.019

Kim, W., Sheets, B. A., & Paola, C. (2010). Steering of experimental channels by lateral basin tilting. *Basin Research*, *22*(3), 286–301. https://doi.org/10.1111/j.1365-2117.2009.00419.x

Landsat Algorithms | Google Earth Engine. (2021). Retrieved from https://developers.google.com/earth-engine/guides/landsat

Langhorst, T., & Pavelsky, T. (2023). Global observations of riverbank erosion and accretion from Landsat imagery. *Journal of Geophysical Research: Earth Surface*, *128*(2), e2022JF006774. https://doi.org/10.1029/2022JF006774

Larsen, E. W., Premier, A. K., & Greco, S. E. (2006). Cumulative effective stream power and bank erosion on the Sacramento river, California, USA[1]. *JAWRA Journal of the American Water Resources Association*, *42*(4), 1077–1097. https://doi.org/10.1111/j.1752-1688.2006.tb04515.x

Latrubesse, E. M. (2008). Patterns of anabranching channels: The ultimate end-member adjustment of mega rivers. *Geomorphology*, *101*(1–2), 130–145. https://doi.org/10.1016/j.geomorph.2008.05.035

Li, D., Lu, X., Overeem, I., Walling, D. E., Syvitski, J., Kettner, A. J., et al. (2021). Exceptional increases in fluvial sediment fluxes in a warmer and wetter High Mountain Asia. *Science*, *374*(6567), 599–603. https://doi.org/10.1126/science.abi9649

Li, Y., & Limaye, A. B. (2022). Testing predictions for migration of meandering rivers: Fit for a curvature-based model depends on streamwise location and timescale. *Journal of Geophysical Research: Earth Surface*, *127*(12), e2022JF006776. https://doi.org/10.1029/2022JF006776

Liang, M., Voller, V., & Paola, C. (2015). A reduced-complexity model for river delta formation–Part 1: Modeling deltas with channel dynamics. *Earth Surface Dynamics*, *3*(1), 67–86. https://doi.org/10.5194/esurf-3-67-2015

Limaye, A. B. (2017). Extraction of multithread channel networks with a reduced-complexity flow model. *Journal of Geophysical Research: Earth Surface*, *122*(10), 1972–1990. https://doi.org/10.1002/2016jf004175

Limaye, A. B. (2020). How do braided rivers grow channel belts? *Journal of Geophysical Research: Earth Surface*, *125*(8), e2020JF005570. https://doi.org/10.1029/2020jf005570

Lininger, K. B., Wohl, E., & Rose, J. R. (2018). Geomorphic controls on floodplain soil organic carbon in the Yukon Flats, interior Alaska, from reach to river basin scales. *Water Resources Research*, *54*(3), 1934–1951. https://doi.org/10.1002/2017WR022042

Martin, H. K., & Edmonds, D. A. (2022). The push and pull of abandoned channels: How floodplain processes and healing affect avulsion dynamics and alluvial landscape evolution in foreland basins. *Earth Surface Dynamics*, *10*(3), 555–579. https://doi.org/10.5194/esurf-10-555-2022

Martin, J., Sheets, B., Paola, C., & Hoyal, D. (2009). Influence of steady base-level rise on channel mobility, shoreline migration, and scaling properties of a cohesive experimental delta. *Journal of Geophysical Research*, *114*(F3), F03017. https://doi.org/10.1029/2008jf001142

Mason, J., & Mohrig, D. (2018). Using time-lapse lidar to quantify river bend evolution on the meandering coastal Trinity River, Texas, USA. *Journal of Geophysical Research: Earth Surface*, *123*(5), 1133–1144. https://doi.org/10.1029/2017JF004492

Mason, J., & Mohrig, D. (2019). Differential bank migration and the maintenance of channel width in meandering river bends. *Geology*, *47*(12), 1136–1140. https://doi.org/10.1130/G46651.1

McFeeters, S. K. (1996). The use of the Normalized Difference Water Index (NDWI) in the delineation of open water features. *International Journal of Remote Sensing*, *17*(7), 1425–1432. https://doi.org/10.1080/01431169608948714

Micheli, E. R., Kirchner, J. W., & Larsen, E. W. (2004). Quantifying the effect of riparian forest versus agricultural vegetation on river meander migration rates, central Sacramento River, California, USA. *River Research and Applications*, *20*(5), 537–548. https://doi.org/10.1002/rra.756

Micheli, E. R., & Larsen, E. W. (2011). River channel cutoff dynamics, Sacramento River, California, USA. *River Research and Applications*, *27*(3), 328–344. https://doi.org/10.1002/rra.1360

Murray, A. B., & Paola, C. (1997). Properties of a cellular braided-stream model. *Earth Surface Processes and Landforms: The Journal of the British Geomorphological Group*, *22*(11), 1001–1025. https://doi.org/10.1002/(sici)1096-9837(199711)22:11<1001::aid-esp798>3.0.co;2-o

Nagel, G. W., de Moraes Novo, E. M. L., Martins, V. S., Campos-Silva, J. V., Barbosa, C. C. F., & Bonnet, M. P. (2022). Impacts of meander migration on the Amazon riverine communities using Landsat time series and cloud computing. *Science of the Total Environment*, *806*, 150449. https://doi.org/10.1016/j.scitotenv.2021.150449

Parker, G. (1976). On the cause and characteristic scales of meandering and braiding in rivers. *Journal of Fluid Mechanics*, *76*(3), 457–480. https://doi.org/10.1017/s0022112076000748

Pavelsky, T. M., & Smith, L. C. (2008). RivWidth: A software tool for the calculation of river widths from remotely sensed imagery. *IEEE Geoscience and Remote Sensing Letters*, *5*(1), 70–73. https://doi.org/10.1109/lgrs.2007.908305

Pekel, J.-F., Cottam, A., Gorelick, N., & Belward, A. S. (2016). High-resolution mapping of global surface water and its long-term changes. *Nature*, *540*(7633), 418–422. https://doi.org/10.1038/nature20584

Repasch, M., Scheingross, J. S., Hovius, N., Lupker, M., Wittmann, H., Haghipour, N., et al. (2021). Fluvial organic carbon cycling regulated by sediment transit time and mineral protection. *Nature Geoscience*, *14*(11), 842–848. https://doi.org/10.1038/s41561-021-00845-7

Rowland, J. C., Shelef, E., Pope, P. A., Muss, J., Gangodagamage, C., Brumby, S. P., & Wilson, C. J. (2016). A morphology independent methodology for quantifying planview river change and characteristics from remotely sensed imagery. *Remote Sensing of Environment*, *184*, 212–228. https://doi.org/10.1016/j.rse.2016.07.005

Sadler, P. M. (1981). Sediment accumulation rates and the completeness of stratigraphic sections. *The Journal of Geology*, *89*(5), 569–584. https://doi.org/10.1086/628623

Sadler, P. M., & Jerolmack, D. J. (2015). Scaling laws for aggradation, denudation and progradation rates: The case for time-scale invariance at sediment sources and sinks. *Geological Society, London, Special Publications*, *404*(1), 69–88. https://doi.org/10.1144/sp404.7

Sah, R. K., & Das, A. K. (2018). Morphological dynamics of the rivers of Brahmaputra. *Journal of the Geological Society of India*, *92*(4), 441–448. https://doi.org/10.1007/s12594-018-1039-y

Scheingross, J. S., Repasch, M. N., Hovius, N., Sachse, D., Lupker, M., Fuchs, M., et al. (2021). The fate of fluvially-deposited organic carbon during transient floodplain storage. *Earth and Planetary Science Letters*, *561*, 116822. https://doi.org/10.1016/j.epsl.2021.116822

Schwenk, J., Khandelwal, A., Fratkin, M., Kumar, V., & Foufoula-Georgiou, E. (2017). High spatiotemporal resolution of river planform dynamics from Landsat: The RivMAP toolbox and results from the Ucayali River. *Earth and Space Science*, *4*(2), 46–75. https://doi.org/10.1002/2016EA000196

Sheets, B. A., Paola, C., & Kelberer, J. M. (2007). Creation and preservation of channel-form sand bodies in an experimental alluvial system. *Sedimentary Processes, Environments and Basins: A Tribute to Peter Friend*, 555–567.

Straub, K. M., Paola, C., Mohrig, D., Wolinsky, M. A., & George, T. (2009). Compensational stacking of channelized sedimentary deposits. *Journal of Sedimentary Research*, *79*(9), 673–688. https://doi.org/10.2110/jsr.2009.070

Strick, R. J., Ashworth, P. J., Sambrook Smith, G. H., Nicholas, A. P., Best, J. L., Lane, S. N., et al. (2019). Quantification of bedform dynamics and bedload sediment flux in sandy braided rivers from airborne and satellite imagery. *Earth Surface Processes and Landforms*, *44*(4), 953–972. https://doi.org/10.1002/esp.4558

Sun, T., Meakin, P., Jøssang, T., & Schwarz, K. (1996). A simulation model for meandering rivers. *Water Resources Research*, *32*(9), 2937–2954. https://doi.org/10.1029/96WR00998

Sylvester, Z., Durkin, P., & Covault, J. A. (2019). High curvatures drive river meandering. *Geology*, *47*(3), 263–266. https://doi.org/10.1130/g45608.1

Tal, M., & Paola, C. (2007). Dynamic single-thread channels maintained by the interaction of flow and vegetation. *Geology*, *35*(4), 347–350. https://doi.org/10.1130/g23260a.1

Torres, M. A., Limaye, A. B., Ganti, V., Lamb, M. P., West, A. J., & Fischer, W. W. (2017). Model predictions of long-lived storage of organic carbon in river deposits. *Earth Surface Dynamics*, *5*(4), 711–730. https://doi.org/10.5194/esurf-5-711-2017

Valenza, J. M., Edmonds, D. A., Hwang, T., & Roy, S. (2020). Downstream changes in river avulsion style are related to channel morphology. *Nature Communications*, *11*(1), 1–8. https://doi.org/10.1038/s41467-020-15859-9

van de Lageweg, W. I., van Dijk, W. M., Baar, A. W., Rutten, J., & Kleinhans, M. G. (2014). Bank pull or bar push: What drives scroll-bar formation in meandering rivers? *Geology*, *42*(4), 319–322. https://doi.org/10.1130/g35192.1

Van Rossum, G., & Drake, F. L. (1995). *Python reference manual*. Centrum voor Wiskunde en Informatica Amsterdam.

Wellmeyer, J. L., Slattery, M. C., & Phillips, J. D. (2005). Quantifying downstream impacts of impoundment on flow regime and channel planform, lower Trinity River, Texas. *Geomorphology*, *69*(1), 1–13. https://doi.org/10.1016/j.geomorph.2004.09.034

Wickert, A. D., Martin, J. M., Tal, M., Kim, W., Sheets, B., & Paola, C. (2013). River channel lateral mobility: Metrics, time scales, and controls. *Journal of Geophysical Research: Earth Surface*, *118*(2), 396–412. https://doi.org/10.1029/2012jf002386

Williams, R. D., Brasington, J., & Hicks, D. M. (2016). Numerical modelling of braided river morphodynamics: Review and future challenges. *Geography Compass*, *10*(3), 102–127. https://doi.org/10.1111/gec3.12260

Wulder, M. A., Loveland, T. R., Roy, D. P., Crawford, C. J., Masek, J. G., Woodcock, C. E., et al. (2019). Current status of Landsat program, science, and applications. *Remote Sensing of Environment*, *225*, 127–147. https://doi.org/10.1016/j.rse.2019.02.015

Xu, H. (2006). Modification of normalised difference water index (NDWI) to enhance open water features in remotely sensed imagery. *International Journal of Remote Sensing*, *27*(14), 3025–3033. https://doi.org/10.1080/01431160600589179

Yamazaki, D., Ikeshima, D., Sosa, J., Bates, P. D., Allen, G. H., & Pavelsky, T. M. (2019). MERIT hydro: A high-resolution global hydrography map based on latest topography dataset. *Water Resources Research*, *55*(6), 5053–5073. https://doi.org/10.1029/2019wr024873

Yang, K., Li, M., Liu, Y., Cheng, L., Duan, Y., & Zhou, M. (2014). River delineation from remotely sensed imagery using a multi-scale classification approach. *IEEE Journal of Selected Topics in Applied Earth Observations and Remote Sensing*, *7*(12), 4726–4737. https://doi.org/10.1109/JSTARS.2014.2309707

Yang, X., Pavelsky, T. M., Allen, G. H., & Donchyts, G. (2019). RivWidthCloud: An automated Google Earth Engine algorithm for river width extraction from remotely sensed imagery. *IEEE Geoscience and Remote Sensing Letters*, *17*(2), 217–221. https://doi.org/10.1109/lgrs.2019.2920225